Application of Fast-neutron Time-encoded Imaging for Warhead Verification

by

Rebecca Elizabeth Krentz-Wee

A dissertation submitted in partial satisfaction of the

requirements for the degree of

Doctor of Philosophy

in

Engineering – Nuclear Engineering

in the

Graduate Division

of the

University of California, Berkeley

Committee in charge:

Professor Kai Vetter, Chair
Professor Lee Bernstein
Professor Michael Nacht
Dr. Peter Marleau

Fall 2020

Application of Fast-neutron Time-encoded Imaging for Warhead Verification

Abstract

Application of Fast-neutron Time-encoded Imaging for Warhead Verification

by

Rebecca Elizabeth Krentz-Wee

Doctor of Philosophy in Engineering – Nuclear Engineering

University of California, Berkeley

Professor Kai Vetter, Chair

Since the height of the Cold War, arms reduction treaties have reduced the number of nuclear weapons from an estimated 70,000 to around 14,000[1]. Future treaties may continue to lower those numbers, address non-deployed or inactive warheads, or address weapon dismantlement procedures. This raises the unique challenge of confirming that items themselves are warheads rather than using a proxy for warheads, such as an entire delivery system. There is a fundamental tradeoff between the confidence a warhead confirmation measurement provides and how intrusive it is. An inspector must have confidence in the accuracy of a declaration of treaty items. If a host's need to limit sensitive information creates measurement requirements that reduce an inspector's confidence in the equipment, then their overall confidence may be worse. We are looking for a solution that enables an "instrusive" measurement while meeting a host's requirements, thus increasing the maximum achievable confidence.

Recent work applied Zero-Knowledge Proof (ZKP) concepts from cryptography to warhead verification as a way to confirm declarations without revealing sensitive information. We developed a verification system using those principles and advanced concepts in radiation detection and imaging, most importantly an advanced rotating mask for Time-Encoded Imaging (TEI) and the availability of stilbene detectors for Pulse Shape Discrimination (PSD). A proof-of-concept fast neutron Time-Encoded Imaging (TEI) system with a cylindrical anti-symmetric mask was built. It demonstrated the ability to distinguish between matching and non-matching items by measuring ^{252}Cf sources and PuO$_2$ hemispheres in several configurations. Simulations were then used to examine the design space of the system shape and size. New metrics and methodology were developed to better evaluate the performance based on the specific tasks of confirming matching objects and distinguishing between different objects. These showed that a thick spherical mask with a large detector performed the best, but changing the shape of the detector or the shape of the mask elements does not improve performance. A second system was built with a mask design based on the outcome of the simulations. As a

spherical mask would have been extremely challenging to manufacture by conventional methods, the mask was 3D-printed using polycarbonate, which was deemed the most suitable 3D-printing material. Measurements with ^{252}Cf sources were used to evaluate its performance and compare with simulations and the first system. It performed well at confirming matching sources and was able to distinguish between sources with more than a 5 cm difference in diameter. The combination of the initial proof of concept measurements, parametric simulation optimizations, and confirming measurements using the second generation system prove the feasibility of this concept as a verification method and its usefulness to future development and deployment.

To my parents, who told me to have scintillating conversation

Contents

List of Figures

List of Tables

List of Abbreviations

3G-AMS Third Generation Attribute Measurement System

AMS/IB Attribute Measurement System with Information Barrier

AVNG Attribute Verification System

BNL Brookhaven National Laboratory

CIVET Controlled Instrusiveness Verification Technology

CONFIDANTE CONfirmation using Fast-neutron Imaging Detection with Anti-Null Time-Encoding

FNMIS (Fieldable) Nuclear Material Identification System

HDPE High-Density Polyethylene

ICBM Intercontinental Ballistic Missile

INF Intermediate-Range Nuclear Forces Treaty

INMM Institute for Nuclear Material Management

LANL Los Alamos National Laboratory

LLNL Lawrence Livermore National Laboratory

MLEM Maximum Likelihood Expectation Maximization

New START Treaty on Measures for the Further Reduction and Limitation of Strategic Offensive Arms

NG-AMS Next Generation Attribute Measurement System

NLL Negative Log-Likelihood

NPT Treaty on the Non-Proliferation of Nuclear Weapons

NTM National Technical Means

ORNL Oak Ridge National Laboratory

PNET Peaceful Nuclear Explosions Treaty

PNNL Pacific Northwest National Laboratory

PSD Pulse Shape Discrimination

SALT Strategic Arms Limitation Talks

SLBM Submarine-Launched Ballistic Missile

SNL Sandia National Laboratories

SNR Signal-to-Noise Ratio

SORT Strategic Offensive Reductions Treaty

START Strategic Arms Reduction Treaty I

TEI Time-Encoded Imaging

TRADS Trusted Radiation Attribute Demonstration System

TRIS Trusted Radiation Identification System

UKNI U.K.-Norway Initiative

WgPu weapon-grade plutonium

WgU weapon-grade uranium

ZKP Zero-Knowledge Proof

Acknowledgments

Thank you to all the people who supported me throughout graduate school and made this thesis possible.

First, to my advisor Kai Vetter, for his insightful comments on my research, his encouragement for me to teach and do outreach, and for fostering a research environment that encourages collaboration in a wide range of areas through the Berkeley Applied Research on the Imaging of Neutrons and Gamma-rays (BeARING). Thank you especially for introducing me to the group I worked with at Sandia National Laboratories.

Second, to Dr. Peter Marleau for his mentorship and the chance to work in such a unique and fascinating research area. I learned so much about not only radiation imaging and arms control, but also how to approach problems with curiosity and creativity.

To everyone I worked with at Sandia: you made it a fantastic and welcoming place to work. Melinda Sweany, Mark Gerling, and Erik Brubaker, for your technical insight and advice. My fellow students, especially Mateusz Monterial, Kyle Weinfuther, and Niral Shah. Kristin Hertz for mentorship, support, and encouragement. Special thanks to Jim Brennan and Dan Throckmorton, who built the CONFIDANTE systems.

To the members of my doctoral committee, Professor Lee Bernstein and Professor Michael Nacht, for their questions, conversations, and feedback.

To all the friends and classmates, for your support and camaraderie, especially: Patricia Schuster, who recruited me to Sandia and has provided invaluable career advice and mentorship; Joanna Szornel, who wrote with me every weekday for seven months of the pandemic; Bethany Goldblum and Ali Hanks, mentors and role models.

To my family, for your love and support. To Paul.

This material was prepared as an account of work sponsored by an agency of the United States Government. Neither the United States Government nor any agency thereof, nor any of their employees, makes any warranty, express or implied, or assumes any legal liability or responsibility for the accuracy, completeness, or usefulness of any information, apparatus, product, or process disclosed, or represents that its use would not infringe privately owned rights. Reference herein to any specific commercial product, process, or service by trade name, trademark, manufacturer, or otherwise does not necessarily constitute or imply its endorsement, recommendation, or favoring by the United States Government or any agency thereof. The views and opinions of authors expressed herein do not necessarily state or reflect those of the United States Government or any agency thereof.

Chapter 1

Introduction

The existence of nuclear weapons poses an existential threat to humanity as any use has the possibility to escalate with catastrophic consequences. However, there are practical realities standing in the way of disarmament. One difficulty is how to verify the dismantlement of nuclear weapons so that all parties have confidence that no one is gaining an unfair advantage. Past nuclear arms treaties have focused on the immediate problem of stability between the two countries with the largest number of nuclear weapons, the United States and Russia. Arms control agreements have reduced the number of nuclear weapons and provided communication and transparency, which enhance stability. At present, the Federation of American Scientists estimates the worldwide nuclear weapon stockpile to be just under 10,000, with another 4,000 retired and awaiting dismantlement [2]. At the height of the Cold War, that number was almost 70,000.

Future arms control treaties will hopefully continue the trend in reduction of numbers but will likely present new verification challengess. At an Institute for Nuclear Material Management (INMM) workshop in 2012 on Preparing for Nuclear Arms Reductions to Address Technical Transparency and Verification Challenges, the participants agreed that the decrease from 1000 to 100 weapons could be a period of instability and that low numbers would require greater openness "to verify that no nuclear weapon state has a strategic advantage because of its arsenal"[3]. The Defense Science Board noted in 2014 that in future arms control, "the requirement for monitoring will begin to emphasize individual warhead or bomb counting" [4]. With large numbers of weapons and focus on deployed systems, verification of prior treaties counted delivery vehicles, i.e. missiles, bombers, and submarines, as a proxy for warhead count. Current and prior treaties have gone so far as to count re-entry vehicles on deployed missiles as part of random short-notice inspections. At small numbers, it will be vital to verify not only the number of weapons deployed, but also inactive weapons in storage. At high numbers of nuclear weapons, a larger uncertainty in the stockpile could be tolerated, but at low numbers the uncertainty must also be low. Removing warheads from the stockpile will

likely require verifying that components and fissile material are disposed of or rendered useless so that a state cannot quickly redeploy a large number of nuclear weapons to gain an advantage over its adversaries. There are various techniques to confirm that containers of warheads contain what they are declared to contain, such as measuring weight or isotopic content, but they must be done without revealing sensitive design information. There is ongoing research in methods to protect sensitive information while still having confidence in warhead confirmation measurements.

Although warhead verification seems potentially far off from being a component of arms control treaty verification, research now can help develop potential concepts and procedures to monitor and verify nuclear disarmament. Understanding the strengths and weaknesses of different concepts will be important when negotiating the use of specific technology to be included in a treaty. As an example, the United States proposed many verification provisions and multiple radiation detection tools for the Intermediate-Range Nuclear Forces Treaty (INF) which the Soviet Union wanted to scale back to be less intrusive[5]. Although the INF ended up including more detailed and intrusive verification measures than previous nuclear arms control treaties, in terms of radiation detection equipment it was fairly simplistic: a simple neutron counter. This same instrument was included in Strategic Arms Reduction Treaty I (START) and Treaty on Measures for the Further Reduction and Limitation of Strategic Offensive Arms (New START). However, that instrument will likely not provide sufficient confidence in the authenticity of a warhead. Substantial technological advances have been made since the 70's and 80's which should be considered, ranging from simple passive detection to advanced concepts in the passive detection of nuclear weapon's specific nuclear signatures or imaging or new means in probing the system and its materials via active means such as NRF or neutron resonance detection. While it is impossible to know what will or will not be accepted by the other party during negotiations, it is prudent to develop and demonstrate new and advanced concepts to address the need for more accurate and effective measures as options for future agreements.

This chapter reviews the verification and monitoring measures which have been implemented in prior nuclear arms control treaties and past research and development of warhead verification methods. Understanding these past efforts will help identify the technological needs for future arms control treaties and the capabilities and limitations of existing verification technology. This leads to the research goals and impact of the work performed in this thesis.

1.1 Monitoring and Verification

A critical part of every treaty is its verification measures. Each party must have the ability to confirm that other parties are complying with the treaty or, inversely, detect non-

compliance. No verification regime is perfect; there is always some risk that activities may go undetected. Past administrations have used the terms "adequate" or "effective" verification, but these are subjective terms with multiple interpretations. Strategic Arms Limitation Talks (SALT) II defined verification as adequate if new weapons development was caught with sufficient time for the us to respond effectively and prevent strategic imbalance. However, other points of view considered any infraction to be a serious issue, no matter how minor or whether they had strategic significance.

Monitoring and verification in nuclear arms control relies on the technical monitoring capabilities of individual parties, known as National Technical Means (NTM). Though NTM have always been a component of verification, they have explicitly been included since SALT I. More recently, cooperative measures such as data exchanges and on-site inspections have been included. Despite being a unique signature of nuclear material, radiation detection has only been used in a narrow context due to concerns about instrusiveness and information security. If a future treaty addresses the inactive or non-deployed stockpile or warhead dismantlement, then the confidence gained by the measurement of radiation signatures might be required to satisfy the verification objectives. This section gives a brief overview of these measures, provides a historical look at the use of radiation detectors in arms control treaties, and outlines the potential need for future warhead verification measures.

1.1.1 National Technical Means of Verification

NTM refers to technology which one country unilaterally uses to verify compliance of another party to the treaty without entering the other country. Satellites are the example many people think of first, but air-, sea-, and ground-based radar, electronic signal collection, and seismic detectors are all examples of NTM. NTM has been explicitly recognized in arms control treaties since SALT I as used by each party and that the other party undertakes "not to interfere with" NTM of the other party and "not to use concealment measures that impeded verification"[6]. Exact capabilities of NTM for each country are not defined in treaties, both because countries do not want their intelligence capabilities widely known and so that the treaty does not limit NTM. The Open Skies Treaty did specify types of cameras and equipment for aerial overflights when it was written in 1992, but as it had no provisions for updating and agreeing to new technology, some considered it to be obsolete when the United States withdrew from it in 2020.

NTM underlies the verification regimes which are then augmented by data exchanges and on-site inspections. Early treaties such as Strategic Offensive Reductions Treaty (SORT) relied on NTM entirely.

1.1.2 Data Exchanges

START and New START call for extensive data exchanges. One important source of information is the transmissions broadcast during missile flight tests, known as telemetry. Telemetry provides information about the launch weight and throwweight of a missile, length of time the fuel burned and time the missile accelerated, and the number of times the missile maneuvered to release reentry vehicles (which during an operational launch would contain nuclear warheads). In the START treaty, the signatories agreed to not encrypt or deny access to telemetry, so the other side could record the data and use it to evaluate missile system capabilities. Additionally, the United States and Soviet Union agreed to exchange tapes of telemetry and other information needed to interpret the data. During the New START negotiations, Russia argued against requiring the broadcast and exchange of telemetry. In the end, the treaty agreed that the countries would exchange telemetry data up to five times each year. Although the telemetry was not considered necessary to verify compliance, the broadcast and exchange would increase transparency and guarantee a degree of understanding of each side's strategic offensive forces.

Another major data exchange is the identity and movement of delivery systems. The United States and Russia maintain a shared database which records unique identifiers for delivery systems by location. Initially only for mobile Intercontinental Ballistic Missiles (ICBMs) under START, the database expanded to all ICBMs, Submarine-Launched Ballistic Missiles (SLBMs), and heavy bombers covered by the limits in New START. When objects move from one facility to another, the database must be updated. The list of objects at a specific facility may then be used by on-site inspectors, who are permitted to "read the unique identifiers on all designated deployed ICBMs or designated deployed SLBMs, non-deployed ICBMs, non-deployed SLBMs, and designated heavy bombers that are located at the inspection site."

1.1.3 On-site Inspections

On-site inspections have been discussed since the beginning of nuclear arms control in 1946, but were not incorporated into treaties until the Peaceful Nuclear Explosions Treaty (PNET) of 1976[7]. Objections centered on inspections being too intrusive and leading to espionage. Now on-site inspections are considered an important part of the verification regime. Air Force General John Hyten, who served as commander of United States Strategic Command from 2016-2019, said that, "we have very good intelligence capabilities, but there is really nothing that can replace the eyes-on, hands-on ability to look at something."[8]

The primary role of on-site inspections is to confirm information gained through NTM and data exchanges. Inspections also foster communication and cooperation and

help ensure transparancy. START and New START both contained multiple types of on-site inspections. START had a dozen types of inspections including facilities, either to confirm the accuracy on the number of items stored at a declared facility or to confirm that eliminated facilities have no treaty related activities. Limited inspection of specific items was also included: distinguishability of nuclear and non-nuclear systems and counting of mobile launchers and missiles. Reentry vehicles on ballistic missiles were also to be counted to confirm the number of warheads deployed, but New START kept the same basic capabilities but categorizes them into Type One and Type Two inspections depending on the type of location. Type One inspections occur at bases that house deployed or nondeployed launchers, missiles, and bombers; Type Two inspections occur at facilities that house nondeployed or converted launchers and missiles. These changes were made to streamline the verification process to make it less costly and complex, but retain inspection capabilities essentially equivalent to the those permitted under START[9].

1.1.4 Radiation Detection Equipment

While radiation detection and imaging is a powerful tool, especially for nuclear material, the concern about intrusiveness is very high. This has led to very limited types of radiation detection instruments. The two that have been used are a neutron counter and a x-ray imager. As x-ray imaging can produce a detailed image, it has only been used to verify the absence of nuclear material, not object confirmation.

These two instruments were first included in the INF, specifically described in Annex IV and V of the Memorandum of Agreement[10]. The INF, which was in effect from 1988-2020, prohibited all ground-launched missiles with a range between 500 and 5500 km. As part of this treaty, the United States and Soviet Union eliminated almost 3000 missiles which would have fallen in this range in the first three years of the treaty. The radiation detection equipment was used to confirm the elimination of some of these missiles. In particular, the Soviet Union had two very similar missiles, the treaty-forbidden SS-20 and the treaty-allowed SS-25. The SS-25 was large enough to contain the SS-20 payload. X-ray imaging was used to image the second stage of the SS-25 missile to ensure that it did not contain an SS-20 missile. The SS-20 carried 3 warheads while the SS-25 only had one. The neutron counter was used to verify the number of warheads inside the SS-25 missiles.

The neutron counter in use was developed by Sandia National Laboratories (SNL) [11]. It has twelve helium-3 gas tubes surrounded by polyethylene blocks. As discussed in 2.2, helium-3 is an excellent detector of slow neutrons; the polyethylene blocks act as moderation so that it will detect fast neutrons. Due to the moderation, the detector is insensitive to the energy of incoming neutrons and functions as a neutron counter.

Radiation detection and imaging techniques have advanced significantly since the INF, but no new systems have been implemented in a treaty due to authentication and verification concerns. Additional neutron counters were tested by the US in preparation for START negotiations, but the INF system was determined to be the best option[12]. START uses the neutron counter that was in INF to inspect designated deployed delivery systems declared to be non-nuclear objects. The neutron counter was redesigned and accepted by the commission as a replacement for use in New START (see New START Protocol: Annex on Inspection Activities, Part Five, Sections 15 and 16).

1.2   Warhead Verification

Future arms control treaties will potentially include new verification requirements like counting inactive weapons or confirming warheads before dismantlement. Current and past treaties have focused on strategic deployed weapons and delivery systems. While there was good reason to do that, the anticipated need of confirming declarations that an item is a warhead means new technology should be researched and developed. This section will outline the reasoning for the past and future verification technology and describe the current areas of warhead verification research and development, grouped by type of information protection concept: attribute, template, or zero-knowledge.

The US and Russia each have 1550 warheads deployed, per the New START limits, and about 2200 more non-deployed and/or slated for dismantlement [2]. Including these in future treaties will require new verification methods to reduce the uncertainty in total numbers and to give credit for dismantling a warhead. A large uncertainty in the number of non-deployed weapons or those designated for dismantlement could cause instability due to the risk of breakout if they were rapidly re-deployed.

The central challenge in developing these systems is balancing the intrusive nature of measurements used for confirmation with the need to protect sensitive information about the design of the weapon. The inspector would like to have as much information as possible in order to have confidence that a declared treaty item is what it is declared to be. The host wants to know that sensitive or classified information about a treaty item will be protected when it is measured in order to protect national strategic concerns and meet obligations under the Treaty on the Non-Proliferation of Nuclear Weapons (NPT). Verification systems must also be authenticated so that parties have confidence that a measurement instrument will behave as designed, measuring and protecting the specified information with no chance that the behaviour could have been changed without the other party knowing. Authentication is usually the concern of the inspector while the host's concern is to certify that information protection measures work as intended and meet the safety requirements of the facility in which it will be used.

One way to meet host and inspector requirements is to use intrusive measurement

techniques but implement an information barrier to protect the sensitive information. Several instruments with information protection barriers have been researched by the United States and other countries[13], [14]. One common concern is the difficulty of authenticating such systems when the inspector cannot see the information being measured. Recently, there have been new concepts proposed based on zero-knowledge protocols in cryptography that design instruments capable of confirming information without recording sensitive information. The following subsections describe the two more traditional types of warhead verification information protection techniques, attribute and template, which both require information barriers, and then the zero-knowledge concept and two of the proposed Zero-Knowledge Proof (ZKP) methods that have been reported in recent literature.

1.2.1 Attribute Methods

Attribute systems measure specific attributes of an item and compare them with an agreed definition of an item (e.g. treaty accountable items contain at least 500 grams of Pu). If the measured attribute is above the minimum threshold, then the item is considered to meet the requirement for positive confirmation. Example attributes are mass and diameter of an item. Systems which measure and calculate attributes have been extensively researched and developed. However, the data collected and the specific value of the derived characteristic attributed to a specific item could be sensitive so there must be some kind of information barrier to protect that information. The threshold value must be insensitive, since it will be known by all parties.

Several developed systems measure the presence of plutonium, plutonium mass, and plutonium isotopics, including: the Trusted Radiation Attribute Demonstration System (TRADS), developed by SNL in the US[15]; the Attribute Verification System (AVNG), developed by the Russion Federal Nuclear Center-VNIIEF, with support from Los Alamos National Laboratory (LANL) and Lawrence Livermore National Laboratory (LLNL), as part of the trilateral initiative [16]–[18]; and a system developed by the U.K.-Norway Initiative (UKNI) [19], [20]. The age of the plutonium and absence of oxide may also be measured, such as with the Attribute Measurement System with Information Barrier (AMS/IB), developed by LANL, LLNL, and Pacific Northwest National Laboratory (PNNL) [21]. The AMS/IB project was followed by the Next Generation Attribute Measurement System (NG-AMS) [22], which determined plutonium isotropics, mass, and age, then by the Third Generation Attribute Measurement System (3G-AMS) designed to measure those plutonium attributes as well as the presence of uranium and explosives [23], [24].

1.2.2 Template Methods

Template systems compare the measurement of a declared item with data collected from a trusted item (i.e. a template). If data collected from a measurement of a presented item sufficiently matches the template data, then the declared item is confirmed. Template methods avoid the need to define what should or should not count as a treaty accountable item. However, sensitive data must still be collected and analyzed, which again implies the need for an information barrier.

The complicated question of how one might produce the trusted data in the template, presumably from a warhead that's been authenticated by some other means, often referred to as a "golden copy", is usually considered a separate problem from designing a template measurement system with information barriers, but suggestions have included measuring a randomly selected deployed weapon or using random choice from a large selection of objects to build confidence. The latter concept will be discussed more in section 2.4.2.

Examples of template systems include the Trusted Radiation Identification System (TRIS), developed by SNL[23], [25]; Controlled Instrusiveness Verification Technology (CIVET), by Brookhaven National Laboratory (BNL)[26]–[28]; and the (Fieldable) Nuclear Material Identification System (FNMIS), by Oak Ridge National Laboratory (ORNL)[29].

1.2.3 Zero-Knowledge Protocols

ZKPs originated in cryptography and refer to a proof which only conveys whether a theorem is true and no other information [30]. In each of these cases, a person could prove they know this information without revealing it by solving a challenge that requires that knowledge. Multiple challenges are necessary; the prover may have some probability of answering the challenge correctly even if their response is false. There are three key properties of ZKP: completeness, soundness, and zero knowledge. *Completeness* means that if the information is true and both parties follow the protocol, then the verifier will be convinced that it is true. *Soundness* means that if the information is false, the prover cannot convince the verifier that is it true. *Zero-knowledge* means that the verifier will not learn anything besides that the initial statement is true or false.

The next three paragraphs are simple examples of zero-knowledge problems: knowing the password to a door [31], the location of a hidden object on the page of a book [32], or the number of marbles in a jar [33].

Ali Baba Cave Suppose there is a cave with two entrances/exits with a password-locked door between them. Alice claims to know the password. To prove her knowledge to Bob without sharing the password, Alice enters the cave. Bob randomly chooses one of the exits and tells Alice to exit from it. There is a fifty-percent chance that Alice entered on the same side as Bob picked, but if they repeat the experience and Alice is

able to exit on the correct side every time, the likelihood that she knows the password increases to the point of acceptance.

Where's Waldo There is a well-known hidden object book series called Where's Waldo in which the reader searches for a specific figure in a busy drawing. Suppose Alice had an algorithm which she could use to quickly find Waldo on any page. Bob might challenge her ability by opening the book to a random page and asking Alice to find Waldo. In order to prove her knowledge but not reveal the exact location, Alice could use a large sheet of paper that hides the size of the book, with an opening that shows Waldo. Bob can see that Alice has found the character, but would neither know the algorithm nor the exact location on the page.

Jar of Marbles Suppose there is a jar full of marbles. Alice claims that she knows the exact number of marbles in the jar, but does not want to tell anyone that number. Instead, she prepares a second jar of marbles with the same number of marbles as the first jar and two buckets with the same number of marbles as each other. To verify Alice's claim, Bob can combine the marbles, pouring one jar into each bucket. The sum of the marbles should be the same no matter which pairs of jar and bucket Bob chooses if the jars did contain the same number of marbles. If Alice did not know the right number, it is very unlikely that the two sums would be the same.

These examples and indeed most ZKP are interactive proofs where a verifier poses a challenge which can only be solved if the prover knows the secret information. Non-interactive ZKP do exist and are the basis of the cryptocurrency zerocash[34]. They rely either on sharing a common, short, random string[35] or using a random oracle model[36]. Non-interactive protocols are not as applicable to a warhead verification process; an interactive challenge with prover and verifier maps well to a host country declaring an object is a warhead and an inspector verifying the declaration.

1.2.3.1 Princeton ZKP

Glaser et al. [33] proposed measuring inspected items with a radiograph using detectors preloaded with the "complement" of a transmission image of a reference item such that after the radiograph, the total fluence is the same in every detector. The image is null; there is no significant deviation from a constant noise value when the detector counts are compared. This is similar to a template approach in testing whether the reference item and tested item match, but using a conjugate template preload means that the measurement result will not contain sensitive information and would not require an information barrier. This was demonstrated using superheated droplet detectors and reference items made of arrangments of aluminum and steel blocks[37].

However, the preloaded detectors must be controlled as a template would, as the image is effectively a conjugate template and would contain design information. Inspectors could not have complete access to the detectors after they were preloaded. Pitts et. al. di-

cuss consideration of the strength of the radiograph: underexposing the detectors could lead to disclosure of sensitive information, while overexposing would not give adequate confirmation of the result. [38] Effective procedures might satisfy these concerns.

1.2.3.2   MIT Resonant Phenomena ZKP

The MIT Lab for Nuclear Security and Policy proposed a physics-based encryption ZKP warhead verification method using transmission X-ray nuclear-resonance fluorescence [39]. In this method, an x-ray beam is passed through a test object; the test object will absorb photons from the beam if they match specific absorption resonances of the nuclei in the object. The outgoing beam then excites a witness foil, which emits resonant gamma rays which are measured by high-purity germanium detectors, which are non-imaging but have excellent energy resolution. The foil thus acts as a physical encryption layer, preventing knowledge of the exact ratio of isotopes in the test object, but emitting the same NRF spectrum for identical test objects in combination with the same foil. In addition to simulation, experiments were done using layers of depleted uranium, aluminum, and High-Density Polyethylene (HDPE) as a proxy warhead, substitutions of lead for hoax objects, and depleted uranium and aluminum encryption foils [40]. In this technique, the inspectors could have access to the detector and resulting gamma spectrum, but not the encrypting foils. Procedures would need to ensure that the foils could not be switched between measurements.

MIT also developed a variation of this concept using epithermal neutron resonance and complement objects (epiZK) [41]. Epithermal neutrons also interact via resonances in the neutron capture cross-sections of actinides. epiZK uses epithermal neutron transmission imaging with a reciprocal mask in the path of the beam to protect knowledge of the item. The resulting image of the combined test object and mask is of a plate with uniform areal density. Proof-of-concept experiments were shown using molybdenum and tungsten targets, which also have neutron resonances in the epithermal region [42]. Again, the inspectors could view the collected data but not the reciprocal masks.

1.3   Goals and Impacts

Applying ZKP to warhead verification led to the development of methods which allow the inspector to view the data at the end of a measurement. However, preloaded data and additional sensitive objects require information barriers and additional procedures and security measures. It would be ideal if a verification system could output a null value at all times during the measurement, so that an inspector could view data as it was collected, and no sensistive data was recorded at any time. P. Marleau and E. Brubaker proposed in 2015 that this could be done using time-encoded imaging [43].

This thesis evaluates the feasibility of fast-neutron time-encoded imaging for warhead verification, studies the systematic uncertainties, and designs an improved prototype.

Chapter 2

Concepts

This chapter provides technical background for the CONfirmation using Fast-neutron Imaging Detection with Anti-Null Time-Encoding (CONFIDANTE) concept, starting with relevant sources and signatures, followed by a discussion of radiation detection and imaging, and concluding with how CONFIDANTE works. CONFIDANTE is a passive imaging system, meaning that it creates an image of the material emitting radiation, as opposed to transmission imaging like x-ray imaging, where radiation from a source passes through an object to create an image, or active, which uses an external source of radiation to activate a material so that it becomes radioactive. This thesis focuses on evaluating the concept using fast neutrons, but gamma rays and slow neutrons are of interest for future work and the principles would apply similarly.

2.1   Radiation Signatures of Nuclear Weapons

The signature which CONFIDANTE measures comes from the radioactive material used in nuclear warheads: uranium and plutonium. Nuclear weapons require fissile isotopes, those that can sustain a fission chain-reaction with fast neutrons. ^{235}U and ^{239}Pu are not the only fissile isotopes but due to factors like cost, ease of fabrication, and radioactivity, they are the fissile isotopes used in nuclear weapons.

Weapon-grade uranium (WgU) has been enriched to have over 90 % ^{235}U compared with naturally occuring uranium, which contains 0.7 % [44]. The remaining uranium is mostly ^{238}U and a little ^{234}U. If the WgU was made by reprocessing uranium from a reactor, it may also be contaminated by ^{232}U, ^{233}U, and ^{236}U. There will likely be contaminants of light elements like carbon and oxygen as well as isotopes of other elements produced by the decay of uranium over time.

Plutonium does not exist in nature by must be produced by uranium in reactors. Weapon-grade plutonium (WgPu) contains about 93 % ^{239}Pu [44]. The remaining plutonium is mostly ^{240}Pu but also contains ^{241}Pu, ^{242}Pu, and ^{238}Pu. Small amounts of ^{236}Pu

Isotope	SF decay mode %	Average neutrons/fission $\bar{\nu}$
U-234	1.6×10^{-9}	1.8000
U-235	7.0×10^{-9}	1.8700
U-238	5.4×10^{-5}	2.0000
Pu-238	1.9×10^{-7}	2.2100
Pu-239	3.0×10^{-10}	2.3200
Pu-240	5.7×10^{-6}	2.2510
Pu-241	2.0×10^{-14}	
Pu-242	5.5×10^{-4}	2.1410
Cf-252	3.09	3.7676

Table 2.1. Spontaneous fission rates and the average neutrons per spontaneous fission in isotopes of uranium, plutonium, and californium [45]. There was no $\bar{\nu}$ value listed for Pu-241.

and ^{244}Pu as well as light elements like lithium, beryllium, carbon, and oxygen may be present.

The predominant source of neutrons in nuclear weapons comes from the spontaneous fission of ^{240}Pu. While other isotopes in WgU and WgPu will decay via spontaneous fission, these sources are orders of magnitude lower both because there is a lower fraction of those isotopes in weapon-grade material, and the isotopes have lower branching ratios for spontaneous fission decay. Spontaneous fission rates for the main isotopes of weapon-grade material are included in Table 2.1. There may also be neutrons produced via (α,n) reactions from alpha decay of uranium or plutonium and light elements like beryllium and oxygen. Since the light elements are only present as trace contaminants, the rate of neutrons from (α,n) is low.

Gamma rays are produced from the isotopes in WgU and WgPu as well as the many daughter products in their decay chains. These isotopes emit gamma rays at hundreds of characteristic energies. For WgPu, the most valuable gamma rays for detection purposes are the 662-keV and 722-keV gamma rays are emitted by ^{241}Am, which decays from ^{241}Pu and the 414-keV and 769-keV lines emitted by ^{239}Pu [46]. For WgU, the dominant emissions in the gamma spectrum come from the daughter products of ^{238}U and ^{234}U. ^{234m}Pa emits gamma rays at 1.001 MeV, 1.399 MeV and 1.832 MeV. ^{214}Bi emits gamma rays at 1.764 MeV and 2.204 MeV. ^{235}U has a prominent emission at 0.186 MeV. These gamma rays are summarized in Table 2.2.

2.2 Fast Neutron Detection

The CONFIDANTE concept can be applied to any radiation signature, but the work in this thesis focuses on fast neutrons, so this section will cover neutron interactions and detection. Fast neutrons are by convention designated as having energy above 100 keV;

Pu/U origin isotope	Isotope	Energy (MeV)
U-238	Pa-234m	1.001
U-238	Pa-234m	1.399
U-238	Pa-234m	1.832
U-234	Bi-214	1.764
U-234	Bi-214	2.204
U-235	U-235	0.186
Pu-239	Pu-239	0.414
Pu-239	Pu-239	0.769
Pu-241	Am-241	0.662
Pu-241	Am-241	0.722

Table 2.2. Notable gamma rays emitted from the decay chains of weapon-grade uranium and plutonium.

slow neutrons are generally below $1\,\mathrm{keV}$. There are two basic techniques to detect fast neutrons: through neutron-induced reations and through elastic scatter. The latter is the mechanism through which organic scintillators detect neutrons. Energy deposited in scintillators produces electronic excitations which de-excite via light emission. This section reviews fast neutron detection methods and organic scintillators.

2.2.1 Detection through neutron-induced reactions

One way to detect neutrons is through neutron capture reactions which result in prompt energetic charged particles. These three are the most widely used because of their high reaction cross sections and the energy of the reaction products (Q-value):

$$^{10}_{5}\mathrm{B} + ^{1}_{0}\mathrm{n} \rightarrow ^{7}_{3}\mathrm{Li} + ^{4}_{2}\alpha + 2.792 \text{ MeV} \tag{2.1}$$

$$^{6}_{3}\mathrm{Li} + ^{1}_{0}\mathrm{n} \rightarrow ^{3}_{1}\mathrm{H} + ^{4}_{2}\alpha + 4.78 \text{ MeV} \tag{2.2}$$

$$^{3}_{2}\mathrm{He} + ^{1}_{0}\mathrm{n} \rightarrow ^{3}_{1}\mathrm{H} + ^{1}_{1}\mathrm{p} + 0.764 \text{ MeV} \tag{2.3}$$

The total cross-sections of the isotopes in these reactions are shown in Fig 2.1. They are most efficient for detection of slow neutrons, but are reasonably efficient even at high energies.

One way to detect fast neutrons with these materials is by placing moderating material around the detector. Incident fast neutrons lose energy through collisions in the moderator and arrive at the detector with lower energy, for which the detector efficiency is higher than the original fast energy. Hydrogenous materials are often used as moderators because more energy is transferred to low mass nuclei per collision; however, since it has a reasonably high capture cross section as well, it is important to optimize the thickness and placement of the moderator. The appropriate amount of moderating
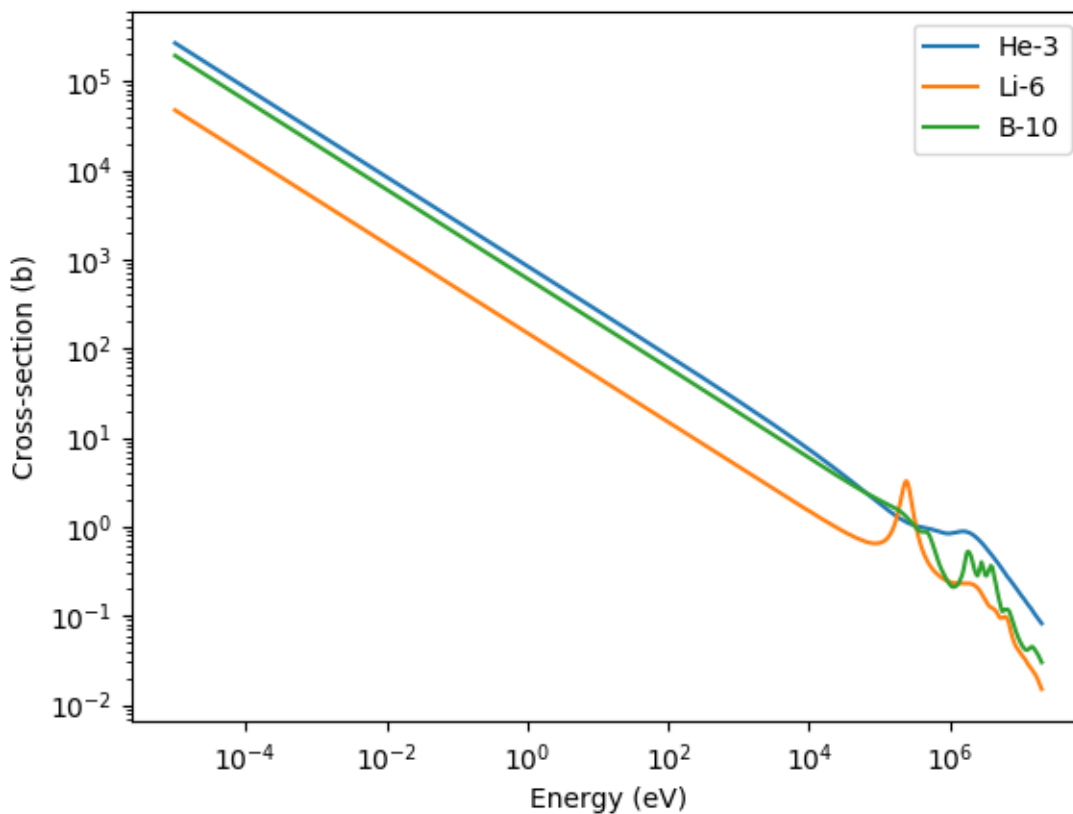
Figure 2.1. Total cross-sections of isotopes commonly used for detection via neutron-induced reaction.

material for maximum efficiency ranges from a few centimeters to tens of centimeters depending on the initial energy of the neutron. This also makes the detector slower in response as time is required for moderation and information about the initial neutron energy is lost.

He-3 and Li-6 can also be used as fast neutron detection without moderation, although the cross section for fast-neutron-induced reactions is orders of magnitude lower than for thermal reactions. This means the efficiency as fast neutron detectors will be much lower than for slow neutrons. However, the detection process is much faster without the time for moderation, on the order of nanoseconds. Additionally, the energy of the incoming neutron may be found by subtracting the Q-value of the reaction from the reaction product energies.

2.2.2 Detection via fast neutron scatter

Fast neutrons may scatter off nuclei without a capture reaction, but this scatter interaction may also produce a signature for detection. Nuclei in the detector are essentially at rest until the neutron elastically scatters and transfers energy. The recoiling nuclei, being heavy charged particles, ionize the material along their path. In some materials, the ionization and recombination can leave molecules in an excited state that emits light as they relax. Figure 2.2 shows a simple cartoon of this interaction. The energy of the recoil nucleus, E_R, depends on the mass of the target nucleus, A, the energy of the incoming neutron kinetic energy, E_n, and the scattering angle of the recoil nucleus, θ, according to the following formula:

$$E_R = \frac{4A}{(1+A)^2}(\cos^2 \theta)E_n \tag{2.4}$$

The maximum fraction of the incoming neutron energy that can be transferred is in a head-on collision where $\theta \cong 0$, thus:

$$\frac{E_R}{E_n}\Big|_{\mathrm{max}} = \frac{4A}{(1+A)^2} \tag{2.5}$$

If the recoil nucleus is ordinary hydrogen (H-1), then the maximum fractional energy is 1. As the recoil nucleus mass increases, the maximum fractional energy transfer decreases. For this reason, light nuclei are preferred for recoil detectors, particularly hydrogen.

2.2.3 Scintillation Detectors

Scintillation detectors are materials which emit light following the absorption of radiation; that is, they scintillate. Compared with other types of radiation detectors, they are known for having higher efficiency but lower energy resolution. They are available in solid, liquid, and gas forms, many of which can be fabricated easily in a large range of sizes and shapes. Organic scintillators, composed of hydrogen and carbon, are good for fast neutron detection based on elastic scattering of neutrons on hydrogen nuclei, or protons, as described in Sec. 2.2.2. In many organic scintillators, like stilbene crystals and commercial liquid scintillators, the fraction of light that appears in the fast and slow components depends on the nature of the exciting particle, which means that PSD techniques can be used to differentiate between particles of different kinds which deposit the same amount of energy in the detector. This ability for particle discrimination is a key factor in choosing a detector for CONFIDANTE to provide accurate neutron counting.

Scintillation in organic materials happens when the recoiling charged particle ionizes the material causing excitations in π-electrons of individual molecules. There are two
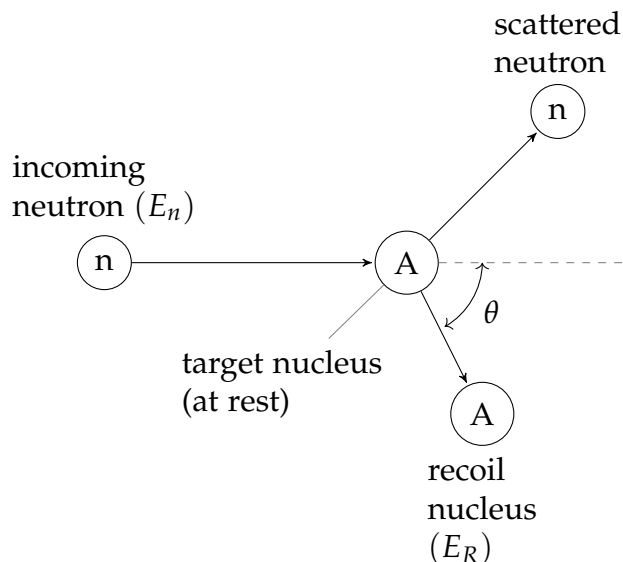
Figure 2.2. Elastic scattering of a neutron off a target nucleus with mass A in the lab reference frame.

types of excitation states: singlet states, where valence electrons have opposite spin; and triplet states, where valence electrons have parallel spin. Direct excitation from ground state to excited states almost always goes to a singlet state, as the triplet is spin-forbidden. Ions may recombine with ionized molecules to form singlet or triplet states; triplet states happen about 75% of the time. Excited states may undergo kinetic processes including de-excitation through light emission. Figure 2.3 shows a diagram of the energy levels in an organic molecule and some of these processes.

The key kinetic processes in organic scintillators follow. *Fluorescence* is de-excitation from the lowest singlet excited state to the ground state via light emission. *Prompt fluorescence* occurs on the order of a few nanoseconds. *Phosphorescence* is de-excitation from the lowest triplet state. Because triplet states are spin-forbidden and come from ion recombination or intersystem crossing from singlet to triplet, phosphorescence occurs more slowly than fluorescence, generally on the μs-ms time scale. Triplet-triplet annihilation causes *delayed fluorescence*. Two triplet states in close proximity may interact to form a ground state and an excited singlet state which de-excites via fluorescence. Triplet states may also be thermally excited back to the singlet state and decay via fluorescence. Two singlet states may also interact and cause a super-excited singlet state and a ground state. Although the super-excited state may still de-excite via fluoresence, the total amount of fluorescence is lower than what would have been produced with the initial two singlet states. This decrease in the prompt light is termed *singlet quenching*.

The likelihood of ion recombination to form triplet states, delayed fluorescence, and
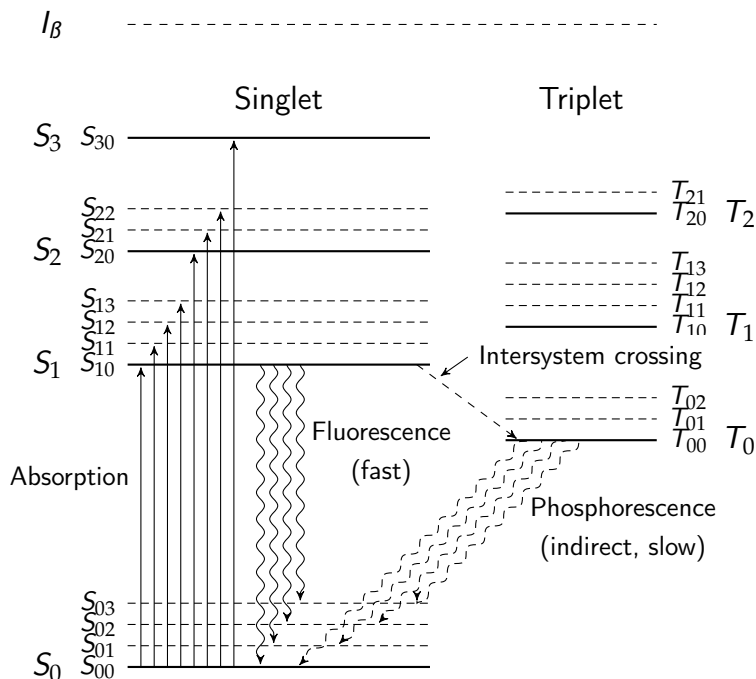
Figure 2.3. Energy levels of an organic molecule with β-electron structure and the kinetic processes which emit light. Adapted from Birks [47].

singlet quenching depend on the density and spatial distribution of excitations. Since different recoiling particles have different dE/dx, depending their mass and charge, the total amount and the time distribution of light emitted may vary. Proton tracks from neutron recoils leave a higher energy density than the electron recoils produced by gamma-ray interactions. A higher energy density increases the amount of delayed fluorescence and singlet quenching, i.e. increasing the delayed light and decreasing the prompt light. This is one of the key advantages of using organic scintillators like stilbene: because the amount of light as a function of time changes with the type of particle, it is possible to distinguish the type of detection by the type of particle.

2.2.4 Pulse Shape Discrimination

Since Several methods exist to quantify these differences and implement PSD. Two common methods are time discrimination and charge integration. In the first, the waveform is integrated and the PSD metric is taken to be the difference in time between two constant fractions of the integrated waveform. Typical values are the time between 0.1 and 0.9 of a pulse or between 0.1 and 0.5 of a pulse. In the second, the PSD metric is the ratio between the amount of charge in different regions of the pulse. Charge integration is often referred to as "tail-to-total" because the most common ratio is the tail region (the

delayed light) of the pulse to the total emitted light, but peak-to-total and tail-to-peak ratios are also used.

Using the charge integration method, this dissertation defined the PSD metric as the ratio of the tail integral to the total integral, where the beginning of the tail window was chosen to maximize the separation between the neutron and gamma bands by optimizing the figure-of-merit (FOM):

$$\text{FOM} = \frac{\mu_n - \mu_\gamma}{\Gamma_n + \Gamma_\gamma}, \tag{2.6}$$

where $\mu_{n,\gamma}$ is the mean of the neutron and gamma bands and $\Gamma_{n,\gamma}$ is the width (FWHM) of the neutron and gamma bands.

An example pulse with lines denoting the start and end of the PSD windows is shown in Fig. 2.4. The start time is defined as the time at 50 % of the leading edge. The total pulse width is 128 samples long and the first 20 samples were used to establish a baseline. Each sample was 2 ns apart. The tail window starts 30 samples after the the start of the pulse, shown in blue. The PSD parameter equals the integral within the tail window divided by the total integral.

When the PSD parameter is plotted against the pulse amplitude, the neutron and gamma events are separated into two bands. An example is shown in Fig. 2.5. The PSD parameter distribution can then be fit by a double Gaussian in slices of pulse amplitude. The solid and dotted lines show the mean and 3σ deviations from the mean. The resulting fit parameters can be used to calculate posterior probabilities using Bayes' theorem for particle identification, defined as:

$$P(\gamma|s) = \frac{f_\gamma(s)R_{\gamma/n}}{f_\gamma(s)R_{\gamma/n} + f_n(s)} \tag{2.7}$$

$$P(n|s) = \frac{f_n(s)}{f_\gamma(s)R_{\gamma/n} + f_n(s)} \tag{2.8}$$

where $f(s)$ are the Gaussian fits, the γ or n indicates the photon and neutron distribution, and s is the PSD parameter. $R_{\gamma/n}$ is the ratio of the estimated counts in the photon and neutron distributions within a light output group. It can either be set using prior knowledge or estimated via an iterative approach [48]. The threshold on the probability to determine whether an event was a neutron was set at 0.99.

2.3 Imaging

Although CONFIDANTE does not record or analyze images directly, the concept grew out of TEI and reconstructed images are included in this thesis to help with qualitative
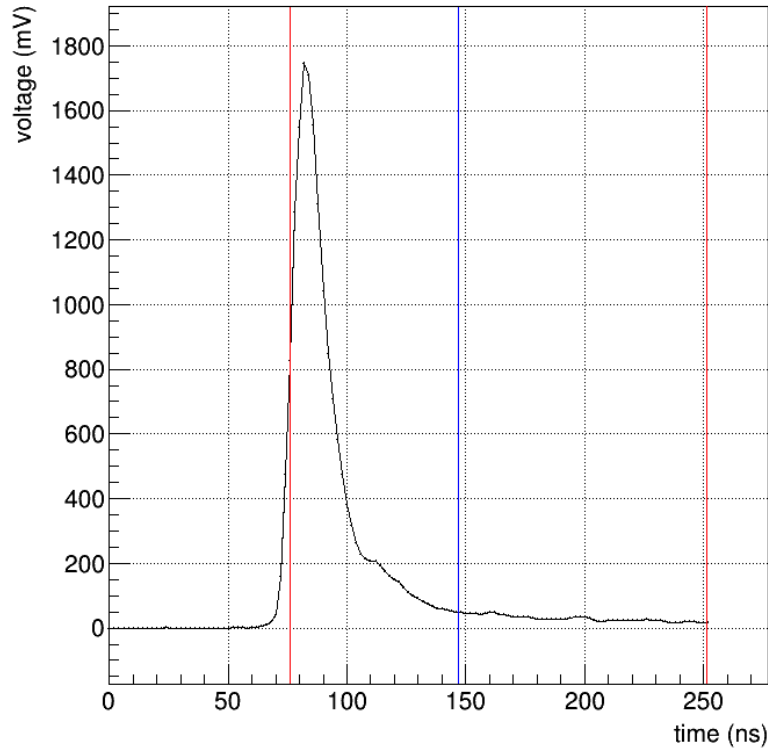
Figure 2.4. Example waveform from the detector used in the measurements for this thesis. The total pulse window is shown in red (from 50 % of the leading edge of the pulse to the end of the pulse at 256 ns) and the start of the tail window is shown in blue (30 samples or 60 ns after the pulse start).

understanding. CONFIDANTE utilizes some unique properties of time-encoded imaging. To understand why and how it works, we will first step through coded aperture imaging, then time-encoded imaging, and end with image reconstruction methods.

2.3.1 Coded Aperture Imaging

Coded aperture imaging was developed to image large areas with weak signals, such as X-ray stars in astrophysics [49]. The challenge was how to improve Signal-to-Noise Ratio (SNR) without worsening angular resolution. With optical imaging, light can be focused with a lens, but gamma rays and neutrons cannot be focused.

Early radiation cameras were similar to pinhole cameras, where a tiny aperture allows signal through and produces an image. The projected image through a pinhol is an inverted view of the field of view. However, the image is faint because a pinhole only
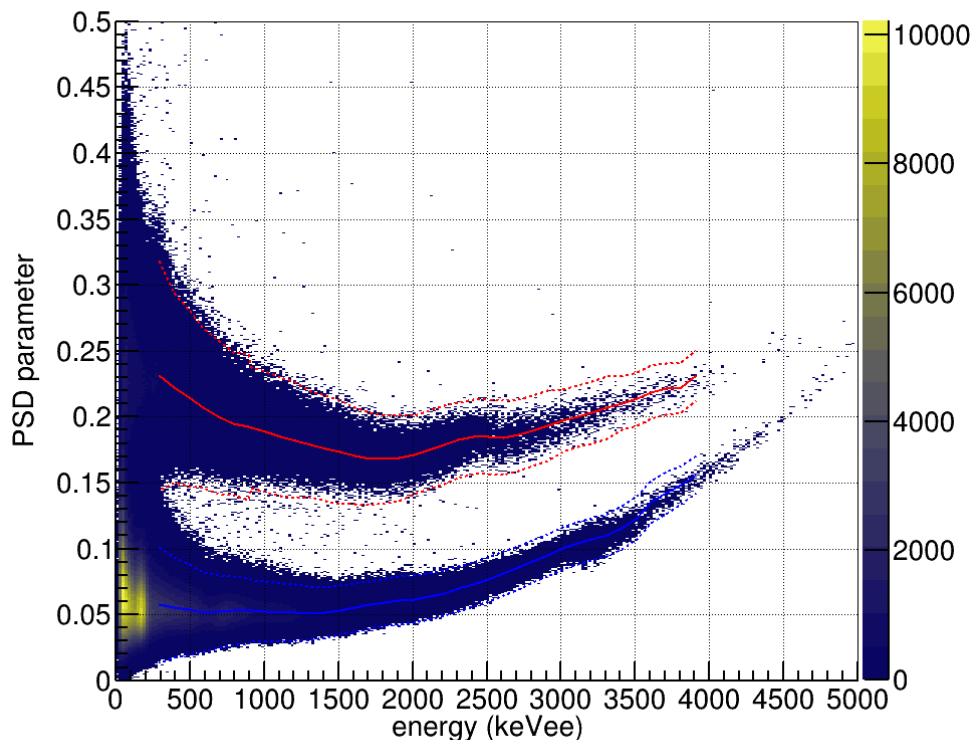
Figure 2.5. Example of plotting the measured PSD parameter vs. the energy pulse. Neutron events lie within the upper band defined by the red dotted lines (the solid red line is the mean and dotted red lines contain 3σ deviations from the mean) while gamma ray events fall in the lower band defined by the blue dotted lines (the solid blue line is the mean and the dotted blue lines contain 3σ deviations from the mean).

lets a small fraction of the signal through. Enlarging the aperture would increase the signal but worsen angular resolution and blur the observation.

Coded aperture uses multiple small apertures; the resulting observation is an overlapping set of projections. The multiple apertures increase the total signal but maintain image resolution. To reconstruct the image of the source, the overlapping images must be deconvolved from each other. A well-designed mask will produce a unique pattern for sources that are separated by the intrinsic angular resolution of the system. With knowledge of the coded pattern of apertures, the detected overlapping pattern can be reconstructed into an image of the original source.

2.3.2 Time-Encoded Imaging

TEI is a method by which the radiation emitted from an item is modulated in time. Rather than modulating the particle flux in space with a fixed mask like coded aperture, TEI uses a moving mask to modulate the particle flux in time. In this implementation, a single detector is surrounded by a cylindrical coded aperture mask[50]. As the mask rotates, radiation from items outside the system are modulated by the pattern of apertures and mask elements on the cylinder. With knowledge of the mask pattern, the time modulated detection rate in the central detector can be used to construct a two-dimensional image of the items.

One key advantage of TEI is that it uses a small number of time-sensitive detectors rather than needing a high channel count and position-sensitive detectors like coded aperture require. Low channel count reduces cost, simplifies the system calibration and integration, and reduces systematic uncertainties. There is a tradeoff between the the angular resolution and sensitivity to the source, however, as the clearest modulation pattern requires that a single mask element must completely block a point source from the detector's view. Small mask elements improve the angular resolution but require a smaller detector, so the efficiency will be lower. This makes this concept most attractive for applications which require high resolution imaging without strict time requirements.

2.3.3 Image Reconstruction Methods

Radiation imaging attempts to reconstruct the source distribution, based on the measurements from one or more detectors.

The key idea with coded aperture imaging is that different source locations will create different patterns of overlapping images or time modulations. For a source in each pixel of the binned field-of-view (a.k.a source space), the detector response can be calculated using forward projection. The complete set of responses for the entire source space we refer to as a response map. A simple backprojection method adds intensity to a reconstructed image based on the probability that a specific event in the detector would have come from each source pixel, based on the response map. Although fast to calculate, backprojection tends to produce blurry images with artifacts. Various corrections and filters may be applied. Filtered backprojection (FBP) usually refers to applying a variation on a ramp filter in order to decrease blurring [51].

Maximum Likelihood Expectation Maximization (MLEM) is an iterative approach which estimates the most likely binned source distribution with a likelihood function that uses a product of Poisson probabilities over a binned set of possible measurements (or observations), given mean expectations calculated according to the estimated system response. An iterative update equation[52] is mathematically guaranteed to return a source distribution with a higher likelihood than the iteration before it. However, the

higher likelihood does not necessarily mean higher image quality. Noise and incomplete or inaccurate response estimation often leads to image artifacts. Because each iteration is mathematically guaranteed to increase the likelihood, one must determine when to terminate the iterations. The number of iterations is a tradeoff between contrast recovery and image noise amplification. The ideal number of iterations stops just before the point where noise in the data or detector response causes high-spatial-frequency oscillations in the reconstructed background. Statistical stopping criteria like minimum change in Poisson likelihood may be used, but it is common to rely on user judgment on the quality of the reconstructed image to choose the stopping point.

MLEM often uses the back-projected source reconstruction as the first step in its iterative approach. With a modeled system response matrix C_{ij} and detected event vectors g_i, backprojection adds intensity according to

$$\lambda_j^{\text{BP}} = C_{ij}^T g_i \tag{2.9}$$

Where λ_j is the source intensity in element j of the image space. In coded aperture, g_i would be the values of counts in each detector pixel. In TEI, g_i is the count values for each fractional rotation of the mask.

The system response matrix is used to forward project the estimate of the neutron source distribution to predicted measurement outcome (in our case, a set of count rates). Then the MLEM algorithm updates the source distribution based on a comparison between the predicted count rates and the measurement. The algorithm for updating is:

$$\lambda_j^{n+1} = \frac{\lambda_j^n}{\sum_{i \in J_j} C_{ij}} \sum_{i \in J_j} \frac{C_{ij} g_i}{\sum_{k \in I_i} C_{ik} \lambda_k^n} \tag{2.10}$$

Where I_i are the set of image pixels that contribute to detector i and J_j are the set of detectors (in coded aperture) or angular bins (in TEI) to which image pixel j contributes.

For TEI, events must first be time-sorted and matched to the rotation angle of the mask. Then MLEM can be used with the two-dimensional source distribution forward-projecting to predict count rate for each rotation angle.

Images presented in this thesis were made using the MLEM algorithm.

ROOT was used to build the detector response matrix for image reconstruction and simulations in this thesis. ROOT is a C++ data processing framework for simulation and data analysis developed at CERN[53]. It provides data structures and mathematical utilities for high-performance statistically sound analysis of large amounts of data.

The detector response matrix was built using a ray-tracing method which accounts for attenuation effects but ignores scattering effects. This simplifies and speeds up the computation. The model of the mask and detector geometry was created in ROOT using TGeo classes. The source space was divided into discrete bins. For a given angular orientation of the mask, the detector response is the average transmission calculated from 1000

trajectories between randomly sampled positions in the source bin to randomly sampled positions within the detector. The path lengths were calculated using the TGeoManager class in ROOT. The attenuation for each path length assumed a neutron attenuation length of 4 cm, determined by averaging the effective attenuation length in HDPE over the neutron energy spectrum of ^{252}Cf. The detector response matrix is a normalized to transform the average transmission calculations into a probability distribution relating a binned source distribution to an observation.

The observation from a TEI system is the detector count rate at each rotation bin; detector counts can either be binned if the mask rotated continuously or the mask may be rotated to discrete angular orientations. The detector response is needed for each rotation bin. Since the mask rotates around a central axis, the detector response for every bin is the same but phase shifted according to the rotation of the mask.

2.4 CONFIDANTE

The TEI system presented here, dubbed CONfirmation using Fast-neutron Imaging Detection with Anti-Null Time-Encoding (CONFIDANTE), was specifically adapted for warhead verification by designing the mask with anti-symmetry such that the pattern on one half of the cylindrical coded mask is the inverse of the other half. When two identical items are positioned on opposite sides of the system, the projection of radiation emitted by one item through the mask is the complement of the projection from a second item on the opposite side at all mask rotation angles; this is true if and only if the two items are identical in the distribution of their radioactive and intervening materials with the angular resolution of the imaging system. Thus, the projections from the two items will sum to an unmodulated constant count rate as the mask is rotated *at all times*.

To illustrate this concept, Fig. 2.6 demonstrates the simplest possible anti-symmetric mask: a half-cylinder. Two items are placed at positions A and B while the mask rotates around detector D. A hypothetical radiation detection rate as a function of time is shown at the bottom of Fig. 2.6. When the aperture is facing item A, the total count rate in the detector has a higher fraction of counts coming from item A than from item B. There may still be some fraction of signal from B because the mask is not perfectly opaque. When the mask rotates to occlude item A, the relative fractions of signal from A and B are reversed. The line in the middle represents the point when an edge of the mask is aligned with the centerline of the two items. As the edge of the cylinder crosses the items, the signals are partially moderated, but still add to the same value. If items A and B are identical, the count rate in the detector as a function of the mask rotation angle will be consistent with a constant count rate (within Poisson counting statistics). If the items differ in shape or activity, then the count rate will exhibit larger variance around the mean value as the mask modulates their signals. Therefore, one way of measuring
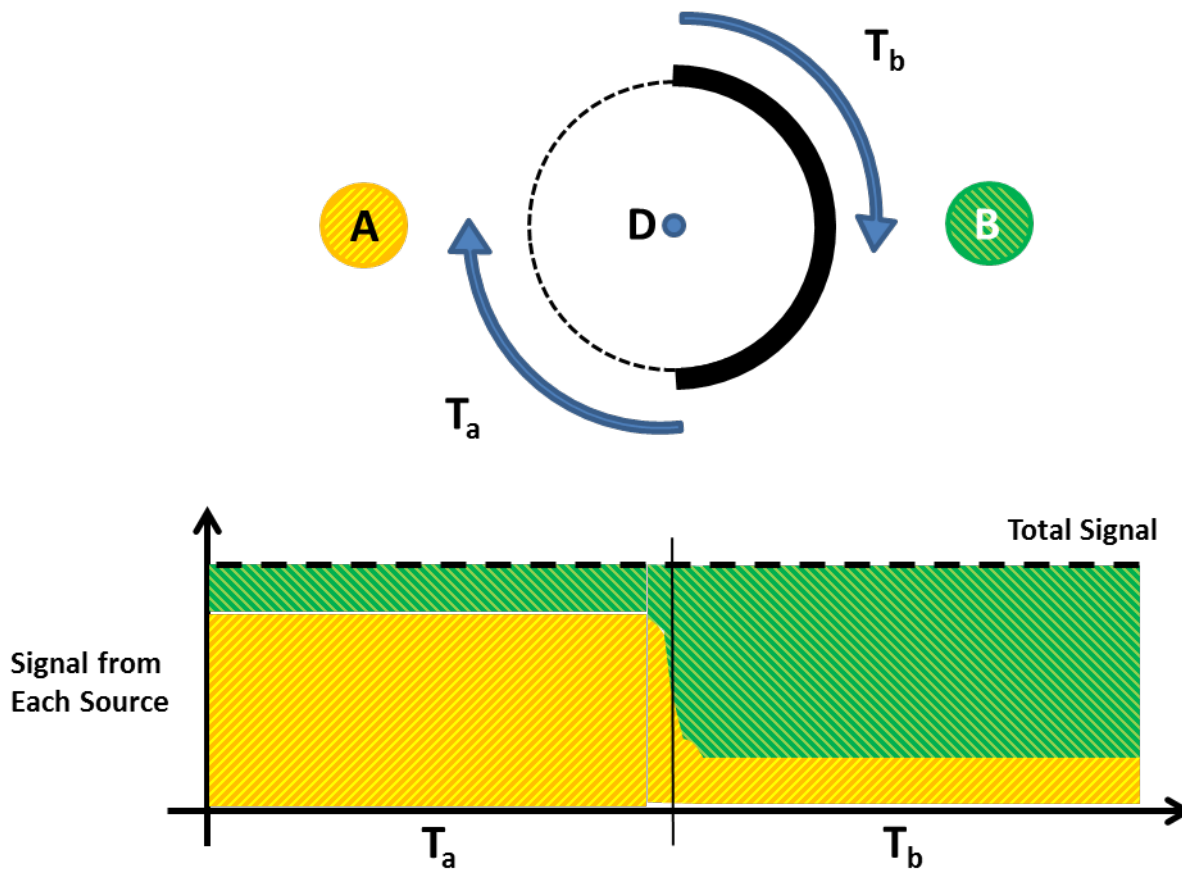
Figure 2.6. An example of the simplest anti-symmetric mask, a half-cylinder. The top shows two items, A and B, on opposite sides of detector D, with the mask rotating around the detector. T_a indicates the open side of the mask is facing item A and T_b when the open side is facing item B. As the mask rotates, the contribution to the total count rate from each item changes but the total count rate stays constant, shown in the bottom plot.

how alike two items are is to measure how closely the distribution of count rates as a function of mask rotation angle follows that of a Poisson-distributed variable. Much of this thesis attempts to quantify how well a single metric can capture the matching to Poisson distribution and what information could be at risk.

A 2D TEI system can be used for this purpose if the mask is anti-symmetric around its center. That is, if there is an aperture on one side of the mask, then the opposite space, 180° around, will have a mask element and vice versa. Thus the system is sensitive to the 2D distribution of radioactive material but will have the CONFIDANTE property where identical objects will produce a constant count rate in the detector. If one would attempt to create an image of a measurement of two identical objects placed 180 degrees apart, it would show only noise.

A potential advantage of CONFIDANTE is that it requires no preloading of data and the constant rate that indicates a null image is present at all times, so theoretically inspectors could have access to the system and data before and during the measurement, instead of needing to keep some equipment or data behind a barrier. Some of the questions this thesis sought to investigate included how precisely the two objects would need to be aligned, what differences could be distinguished, how long it would take to have confidence in whether objects matched or not, and what information might be at risk. The system as presented allows one to determine the total number of detector counts per second, so it is not completely zero knowledge. It is also important to understand the impact of the thickness of the mask and detector on the modulation of the signal. Crossing points where the path of a particle interacts with less than the full thickness of the mask will result in partial transmission from one side, contrary to an ideal modulation pattern which either has zero transmission or full transmission at a time. Partial transmission would cause the sum to be higher or lower than expected and deviate from the constant rate.

2.4.1 Types of particles

The CONFIDANTE concept could theoretically be applied to any particle. The choice of particle would affect the material of which the mask was made and the type of detector. Based on the discussion of weapon-grade plutonium and uranium signatures, fast neutrons and gamma rays are the obvious choices, but slow neutrons or even a form of active interrogation have been suggested. While this thesis will only focus on one type of particle, a system sensitive to multiple types or having multiple types of systems would increase confidence in the measurements.

2.4.1.1 Fast Neutrons

Fast neutrons are a distinctive signature of transuranic material. The fission spectrum primarily produces fast neutrons, so they occur at a higher rate than slow neutrons.

The neutron energy spectrum from different fission sources is difficult to distinguish. This is potentially a downside, as different fissionable material would look similar to CONFIDANTE, but it was also useful for initial proof-of-concept measurements using lab sources. Ideally, a fast neutron system could be used in conjuction with a gamma system.

2.4.1.2 Slow Neutrons

Slow neutrons are produced at a lower rate from fission, but are potentially interesting in conjunction with other types. For example, there are newer types of scintillators which are good for gamma ray detection but also doped with elements like lithium to enable

slow neutron detection. A mask designed for slow neutrons might be achieved by a thin layer of a neutron capture material like boron on the inside of a mask designed for fast neutrons or gamma rays.

2.4.1.3 Gamma Rays

Gamma rays are potentially a better fingerprint than neutrons since gamma ray energies are specific to the isotope that produced them. However, saving a full gamma spectrum would reveal too much information. One potential path would be to only save the counts in given energy windows. They would need to be carefully chosen so that they were specific enough to be useful without saving too much information.

A gamma system has two major advantages. First, good attenuation materials for gamma rays, like tungsten or lead, have much smaller attenuation lengths. This means the mask could be thinner, which improves imaging performance and could decrease the overal system size. Second, the source strength will be much higher for the same amount of material. The rate of gamma decay for both special nuclear material and lab sources like Cf-252 is much higher than the neutron production rate. This would decrease the total amount of time needed to measure objects, since the measurement time is dependent on the number of counts needed to meet statistical requirements. There are potential new mask designs as well: a thick mask which provides better collimation or a multi-layered mask could still have high enough count rates to complete a measurement in a reasonable amount of time.

2.4.1.4 Active Interrogation

Since CONFIDANTE uses passive imaging and a single small detector, the efficiency is quite low even before one factors in the low neutron emission rate. One potential method to increase the signal is to use some kind of active interrogation, where a source is used to induce fission in the sample. While in theory this would be helpful by increasing the signal strength, it would also add noise from neutrons detected directly from the interrogating source.

2.4.2 Concept of Operations

One inspection paradigm is for the inspector to be allowed to arbitrarily pick two objects from the set of treaty items declared to be alike. Those two items would then be tested using CONFIDANTE to determine how well the distribution of radioactive material matches. The randomness introduced by the inspector choice decreases the likelihood that the set contains hoax items. This process could be repeated an arbitrary number of times. As more objects are tested, the confidence that all the objects match is increased. Objects may either be compared with a true warhead or could be compared pairwise

within the set of declared items. Comparing with a true warhead does of course give higher confidence in the specific tested object. Comparing pairwise within the set lessens the burden of having a true warhead present, but also lessens confidence in the set of objects. At some point the number of matching objects could be large enough that the cost or difficulty in making false objects is prohibitive. In order to have complete confidence in the tested objects, they must be compared with a true warhead. If many objects have been linked by pairwise comparisons, then they are all effectively compared to the true warhead if even one measurement is made with one. They they all become true warheads, any one of which can be used to compare against a new declared item.

Random choice may also be used with measurement systems: identical copies of the system or of individual components could be manufactured and one or more be chosen by the inspector for use. While random selection does not remove the need for validation, it does improve confidence in the moment and potentially move the time and place for validation [54].

2.5 Conclusion

Based on these considerations, we built a fast neutron system to prove the concept worked as described and begin to probe some of the questions posed in Section 2.4 The next chapter describes the system and the measurements for which it was used.

Chapter 3

Feasibility

This section describes the proof-of-concept system and the measurements and evaluation of results done with it to prove the feasibility of this method.

3.1   Proof of Feasibility System Description

A two-dimensional anti-symmetric mask had been designed with the same geometric properties (mask radius, aperture sizes, mask thickness, etc.) as the proof-of-concept 2D-TEI system in [55]. Figure 3.1 is a photo of the proof-of-concept CONFIDANTE system from the side.

The mask comprised a stack of nineteen 1.9 cm thick sheets of High Density Polyethylene (HDPE) cut into a cylindrical mask/aperture pattern by water jet from a single piece. Each mask element was a wedge with angular width of 2.4 degrees, inner radius of 44.92 cm and outer radius of 55.08 cm. The top and bottom rows did not contain any apertures. The aperture pattern with the best modeled imaging performance out of 100 randomly generated anti-symmetric patterns was selected. Best imaging performance was defined by a χ^2 value between reconstructed images and true images used as an input to Monte Carlo simulations. The true image test patterns used were 20 cm diameter circular ring sources at 5 different vertical displacements: (0,20), (0,10), (0, 0), (0, -10), and (0, -20).

With appropriately sized central detectors, this mask design had an expected intrinsic angular resolution of 2.5° in both horizontal and vertical dimensions. Fig. 3.4 shows the MLEM reconstructed image (with 20 MLEM steps) of a single ^{252}Cf point source at 1 m for a 3.3 h measurement. The FWHM of this image is smaller than the 1° binning used in the image histograms. Based on measurements with the 2D-TEI system, two point sources separated by 2° could not be separated but could be distinguished from a single point source in 12 h [55]. This is sufficient for the purpose of testing CONFIDANTE. The items of interest are on the order of tens of centimeters. The goal of

CONFIDANTE is to confirm whether items match within some tolerance; for this size item of interest, resolution on the order of centimeters is reasonable.

Along the axis of the cylindrical mask were two 2.54 cm diameter, 2.54 cm deep cylindrical stilbene organic scintillator detector pixels coupled to 5.08 cm Hamamatsu model 6094 photomultiplier tubes (PMTs) made by Inrad Optics. The centers of the detector pixels were positioned 5.08 cm above and below the centerline of the mask (detectors are labeled 0 and 1, respectively). The current signals from the PMTs were digitized by a Struck SIS3316 250 MHz, 14-bit digitizer and read out via USB by a laptop PC. The detectors were calibrated with a sensitive energy range of 50 keVee to 2 MeVee. Because the detector rates are compared to themselves over time rather than each other, matching their relative gains was not important.

The mask position was tracked using a rotary encoder connected to the mask with a rubber wheel. Its position was read by USB in a separate thread. A metal divot attached to the rotation table passed over a switch on the stationary mask frame to mark the end of one rotation and reset the encoder. The digitizer and computer clocks were synchronized at the beginning of each measurement and are used to assign a mask angular orientation to every recorded event. The computer clock was read out with the encoder position. Best results were found with several short measurements digitally added together; in measurements of more than a few hours, the two clocks could become out of sync. Computer clocks keep time using crystal oscillators and network time protocols and are thrown off by many factors, such as network jitter, software delays, and environmental conditions [56]. Even a few thousandths of a second disparity per hour adds up over several hours to be significant. Making several short measurements ensured that the clocks were synced frequently.

3.2 Analysis Methods

3.2.1 Data Processing

The proof-of-concept system output a ROOT file with two streams of data written as TTrees, one from the digitizer and one from the motor encoder. The digitizer output included a waveform and time stamp using the digitizer clock for each event in the detector. The motor output saved the motor encoder position and corresponding time stamp from the laptop clock.

Python scripts processed that output to obtain the pulse height, time stamp, mask position, and probability of being a neutron or gamma-ray for each event. The pulse height was defined as the maximum height of a waveform minus a baseline value. The baseline was estimated as the average of the first 20 samples. The mask position for an event was estimated by using the motor position and time stamps to interpolate
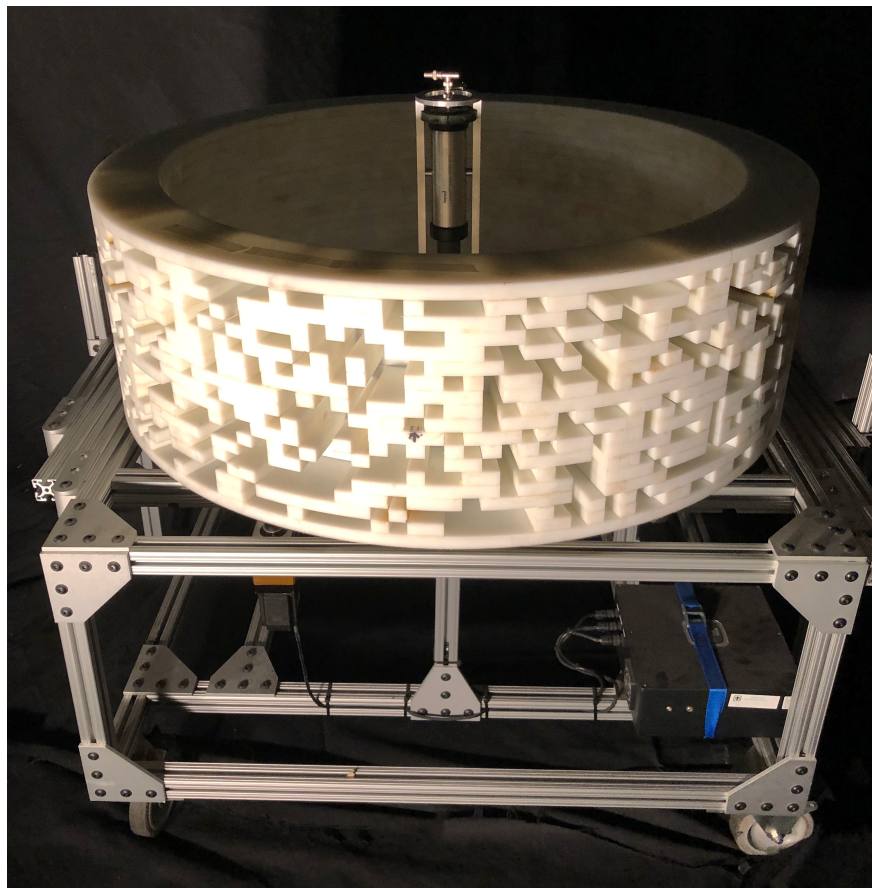
Figure 3.1. A photo of the proof-of-concept CONFIDANTE system.

the instantaneous position for digitizer time stamp. Pulse shape discrimination (PSD) using integrated charge comparison was used to separate gamma-ray and fast neutron detection events. This produced a histogram of the neutron counts as a function of mask rotation angle with $1°$ bins. Due to uneven amounts of time spent accelerating and decelerating, as well as slippage in the drive wheels, the dwell time as a function of of rotation angle is not constant. The neutron count was corrected by dividing by the time spent at each angle read out by the encoder. In order to quantify whether objects on opposite sides of the mask matched or not, two metrics were calculated. The MLEM algorithm was used to reconstruct a two-dimensional image for a few measurements.

3.2.2   Evaluation Metrics

Two metrics were used to evaluate the observed data. The goal was to quantify whether the data were consistent with a constant count rate with only Poisson-distributed noise, i.e. no other modulation was present.

3.2.2.1 Feynman-Y

The Feynman Y value (FY) is defined as the ratio of the distribution's variance to its mean minus 1.

$$FY = \frac{variance}{mean} - 1 \tag{3.1}$$

A Poisson distribution has a variance equal to its mean value and therefore has a Feynman Y of zero. The Feynman-Y is a direct test of whether the number of counts as a function of angle has a Poisson distribution around a constant mean. A smaller FY value indicates the distribution is close to Poisson and therefore the two sources are matching. A larger FY value means the distribution is not Poisson and the two sources are not matching. The exact threshold for distinguishing FY values is unclear. Preliminary studies suggest an operating point between 0.1 to 0.9 might be suitable [57]. It will depend on the desired rate of false negatives.

This was the first metric we considered as it would be simple to measure and calculate. It had the potential for real-time updating as measurements were being done.

3.2.2.2 Chi-squared Test and p-values

As a second way to test if the count rate was statistically consistent with a constant rate, a reduced χ^2 and p-value were calculated.

The χ^2 test measures the goodness-of-fit between observed and expected values and is defined as

$$\chi^2 = \sum_{i=1}^{N} \frac{(O_i - E_i)^2}{E_i} \tag{3.2}$$

where O_i is the observed count value for angular bin i and E_i is the expected count value for angular bin i. The expected count value is taken to be the mean over all mask rotation angle bins. The reduced χ^2 is the χ^2 value divided by the number of degrees of freedom. Since the rotation angles were binned into 360 one degree bins, the number of degrees of freedom is 359. A reduced χ^2 value close to 1 indicates the count rate is close to constant, i.e. that the items match.

The p-value is the probability that the statistical summary when the null hypothesis is true is the same as or greater than the statistical summary of the observed results. In this case the statistical summary is the χ^2 value. If the p-value is very low, the observed results are extremely unlikely if the null hypothesis is true, and so the null hypothesis is rejected in favor of an alternative hypothesis. In our system, the null hypothesis is that the count rate is constant as a function of rotation angle which is indicative that the two items are identical. The alternative hypothesis is that the count rate contains excess variance over expected statistical fluctuations which is indicative that the two items are

not identical. That is, if there is only a source on one side of the mask or if the sources are different on the two sides of the mask, the p-value will be low. If the p-value is higher, the data is consistent with the null hypothesis. Typically, the null hypothesis is accepted with p-values above 0.05. This sets a clear threshold for matching versus non-matching object data.

This metric could be applied in two ways to CONFIDANTE. If two objects matched, the counts per angle bin should be constant within a Poisson distribution. First, the observed counts per angle bin can be compared with a constant flat distribution. In that case, the expected value for a measured data set was set as the mean counts per bin. Second, the binned distribution of counts in all of the 1-degree angular bins can be compared with that expected of a Poisson distributed variable with the same mean and integral as the binned data. That is, since the Poisson distribution probability mass function is:

$$p(n) = \frac{\mu^n e^{-\mu}}{n!} \tag{3.3}$$

Where μ is the mean value. This takes into account the noise, but requires additional analysis steps.

Examples of these concepts can be seen in Fig. 3.2 and Fig. 3.3. The red lines are the expected values (mean value or Poisson distribution, respectively) and the black dots are observed data.

3.3   Cf-252 Experiments

Several measurements were made using two 19.91 μCi Cf-252 sources. Three sources were purchased whose activities were certified to match within 5 %. Two of the three sources were measured to match within 1 % of each other; these were the sources used in this study. Each source is in a capsule of 8 mm by 47 mm, but as they contain nanograms of material, the actual material is much smaller and approximates a point source. The ^{252}Cf sources were used for a basic comparison of a single source vs matching sources, misalignment of the source, and using the sources to trace out shapes as a substitute for extended sources. Sources were aligned with the center row of the mask using a laser pointer which fit inside one of the mask openings. This worked very well for height alignment but had uncertainty in angular placement. The pointer was placed in an opening in the center of the mask and the command run to move the mask a given number of degrees, e.g. to align sources at 90 degrees and 270 degrees, the mask was rotated 90 degrees, then 180 degrees. The encoder had an average of 60,000 steps per 360 degree rotation and had a physical trigger to accurately set the zero degree point, but individual movements could vary by several steps.

3.3.1 Single Source Comparison

Measurements were made with a single source on one side of the mask, to illustrate the modulation from a single object, and with one source on each side of the mask, to show how matching sources create a flat distribution of counts. The first results are presented for a single ^{252}Cf source on one side of the mask. When a single item is placed next to the system, the count rate in the detector exhibits modulation as the mask rotates across the line of site to the source. That count rate as a function of mask rotation angle is shown in Fig. 3.2a. The red line is the mean value of counts per unit angle. When the number of counts per unit angle are histogrammed, as in Fig. 3.3a, they are clearly not Poisson distributed. A Poisson distribution with the same mean and area as the counts histogram is shown in red.

A matching Cf-252 source on the opposite side of the mask created by taking existing statistically independent data from the same measurement and adding a 180° phase shift to every event. This data is shown in Fig. 3.2b and Fig. 3.3b. When the shifted data and original data are summed together, in the way that two identical sources on opposite sides of the mask would sum, the number of counts is consistent with noise. This is seen in both Fig. 3.2c, the plot of the counts versus mask rotation angle, and Fig. 3.3c, the histogram of counts per unit angle. It is evident that the data follows a Poisson distribution around some constant mean value by comparing it to the red lines, which again are the mean value of counts per angle and the expectation for a Poisson distributed variable centered at that mean with the same area as the total number of counts.

In order to quantify how close the count rate is to constant as a function of rotation angle, the goodness-of-fit was estimated using a reduced χ^2 test. A reduced χ^2 value equal to 1.0 indicates a perfect fit (see Statistical Methods section). The results for these Cf-252 measurements are found in Table 3.2. As expected, the matching sources have a low reduced χ^2 value of 1.03 while the single source values are 5.12 and 4.95. The p-value for the two matching sources case have a p-value of 0.3230, which means it is consistent with the null hypothesis, i.e. the count rate is constant. For the single source cases, the p-values are 0.000 which are inconsistent with the null hypothesis, i.e. the count rate exhibits modulation and there are not matching objects.

Though the construction of images from these measurements is unnecessary to the problem of verifying that two items are identical, it is instructive to demonstrate that 1) the system is a functional imager and 2) it is not possible to produce an image when the measurement is consistent with noise. Fig. 3.4 shows the reconstructed images of the single source and matched sources using MLEM [52]. When there are two maching sources directly across from each other, the reconstructed image is consistent with noise.
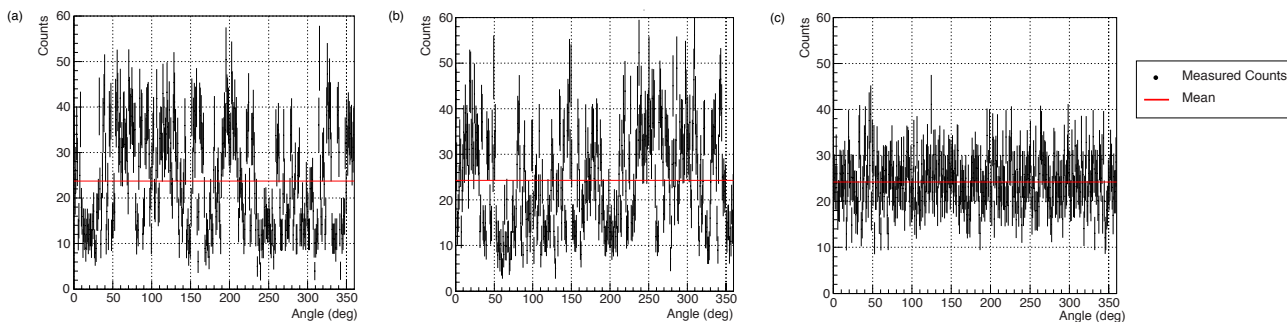
Figure 3.2. Count rate in the detector as a function of mask rotation angle for a small 19.91-μCi Cf-252 source. The red line is the mean value of counts per angle. A single point source clearly shows modulation pattern of the mask. (a) Cf source on one side of the mask (b) Cf source with a 180 degree phase shift (c) Cf sources on both sides of the mask.
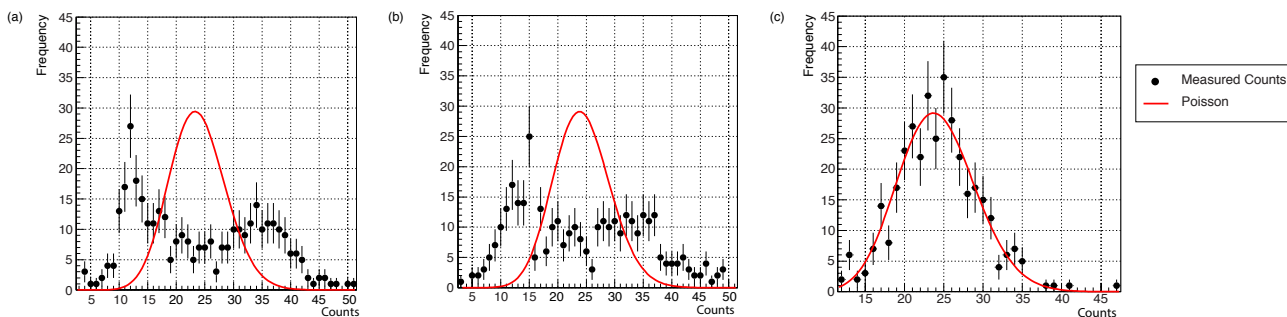
Figure 3.3. The distribution of counts per unit angle for a single Cf-252 source. The red line is the expectation for a Poisson distributed variable with the same mean and integral value as the data. (a) Cf source on one side of the mask (b) Cf source with a 180 degree phase shift (c) Cf sources on both sides of the mask.

3.3.2 Misalignment Experiments

This set of experiments placed Cf-252 sources on opposite sides of the mask. One source was moved from exactly opposite the first source (i.e. a zero degree misalignment) to a small misalignment of 0.0°, 0.5°, 1.0° and 2.5°. This was measured with the use of a laser pointer set in an aperture pointing out of the mask: the laser pointer was set in the mask and rotated from 0° to the desired angular position and the source was placed so the laser pointer hit it in the middle. The distance from the outside surface of the mask to the source was kept constant. The metric over time was calculated to understand how the amount of time (that is, the total number of counts) impacted the metric and if there was a minimum time to distinguish between objects.
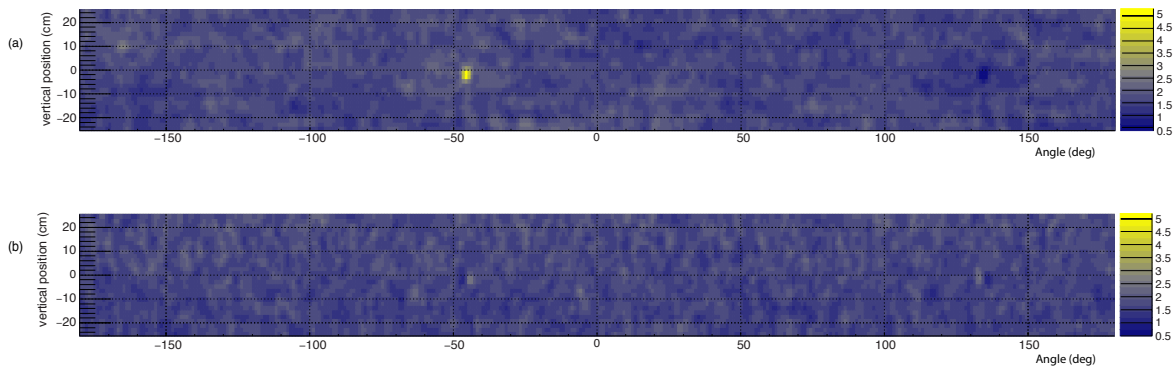
Figure 3.4. Image reconstruction using MLEM for (a) Cf source on one side of the mask (b) Cf sources on both sides of the mask.

Figure 3.5 shows the Feynman-Y as a function of time for measurements of the ^{252}Cf sources on opposite sides of the mask with misalignments of 0.0, 0.5, 1.0 and 2.5; as well as a measurement of a single Cf-252 source. The single source is clearly different than aligned sources; the FY is above 1 by the second hour and continues to increase over the entire measurement. The 0.5° and 1° misalignments are unable to be distinguished from the aligned sources for the length of dwell times explored here, but the 2.5 degree misalignment is distinguished as misaligned due to the higher FY values. It is likely that there was more uncertainty than expected in the precision of the misalignments. As mentioned, the mask was rotated with a laser point to align each source. The mask has a physical home switch which resets the encoder position after a full rotation to keep the measurements consistent, but moving the mask less than a full rotation causes inconsistencies with the encoder. There turned out to be uncertainty in the encoder position on the order of 0.5° to 0.3°. Newer motors are more precise and do not slip if the motor pauses at a position, so this can be fixed in future systems. The 2.5° misalignment looks like it can be distinguished, as the FY increases for the first several measurements, but it decreases by the end of the measurement. It is still higher than the other configurations, but this is not the expected behavior. It could be that position uncertainty made the configuration closer to a 2° difference than 2.5°. More investigation needs to be done into the sensitivity of differences between objects.

3.3.3 Shape Matching Experiments

Another set of experiments used a stage to move a Cf-252 source and trace out 2D images of squares and circles. This was useful to consider extended sources of different shapes when such shapes were not available. The stage had two stepper motors which
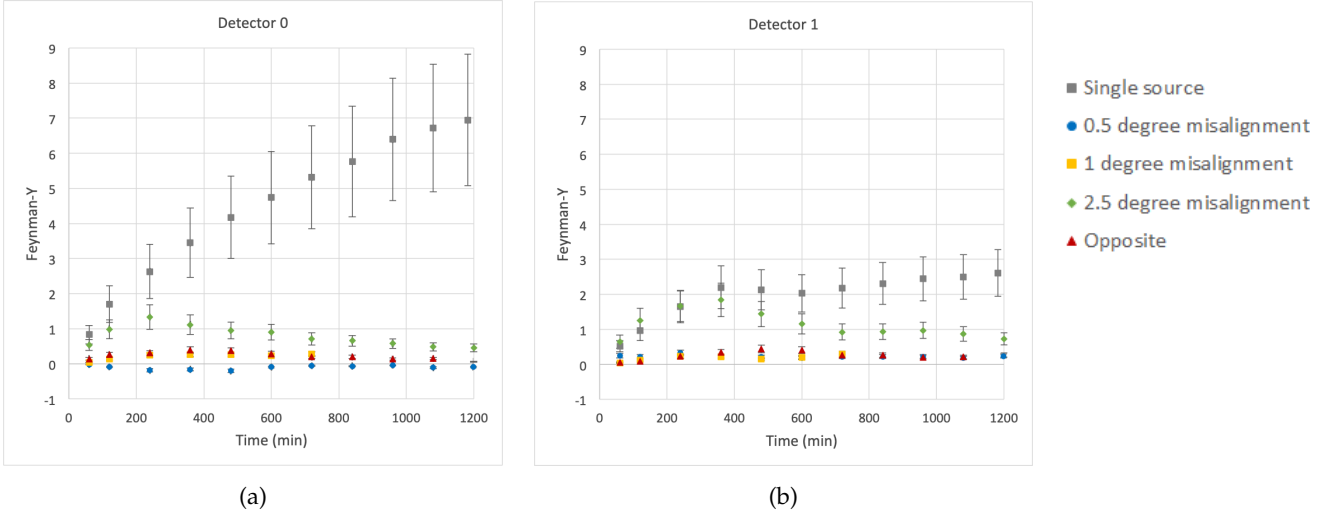
Figure 3.5. Feynman-Y vs. dwell time for (a) top detector and (b) bottom detector for a single source and two sources misaligned by 0.0, 0.5, 1.0, and 2.5 degrees. Error bars represent 3σ uncertainty in the FY.

controlled movement along vertical and horizontal axes. It was run with custom python code. Since only one stage of this type existed, measurements were paired during the analysis by adding a $180°$ phase shift to one measurement. This also removed any uncertainty from the alignment of the items. The objects traced out included circles with diameter of 12.19 cm, 16.26 cm, 20.32 cm, 24.38 cm and 28.45 cm and squares with side length 16.26 cm and 20.32 cm. All objects were tested paired with a measurement of the same size object. Circles and squares with the same size parameter were compared, as they would be closest in size. The smallest circle was also paired with every other measurement.

Table 3.1 shows the results of different combinations of shapes with different dimensions (digitally added together in post-processing). Fig. 3.6 shows the MLEM reconstruction of four of the shapes. Note that the metrics presented in the table are based upon the counts from the raw data and do not require image reconstruction. Images are purely for reference to aid in understanding. The images and results are based on a 1000-min dwell time.

An additional metric is included here which measures the χ^2 and p-value, where the null hypothesis is the count rate as a function of angle being constant. A p-value of less than 0.01 is considered significant and rejects the null hypothesis. Therefore, for the first set of shapes, which are matching, a low Feynman-Y and high p-value are expected; the
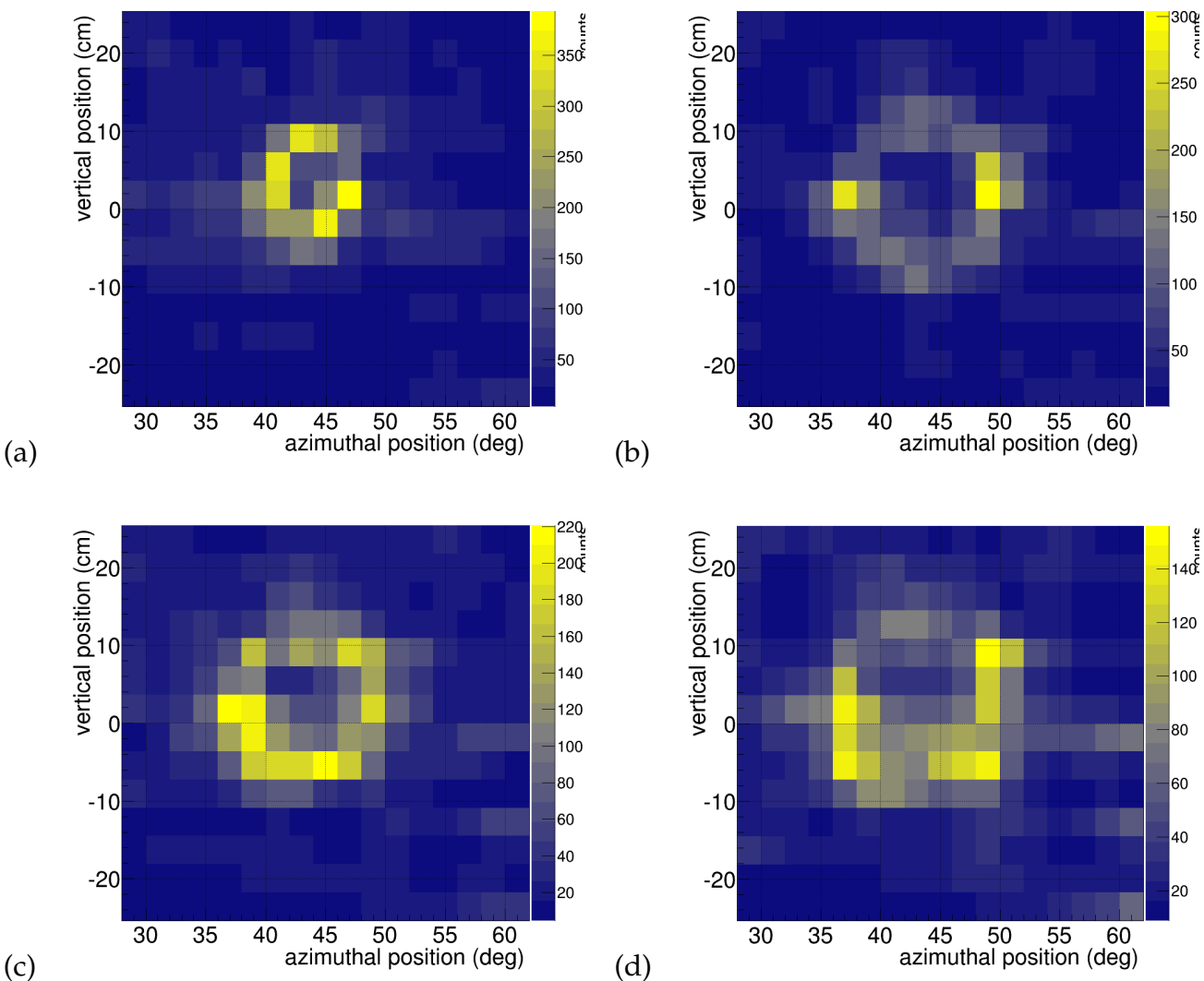
Figure 3.6. MLEM reconstructions of the 12.92 cm circle (a), 20.32 cm circle (b), 16.26 cm square (c) and 20.32 cm square (d) after 1000 min.

inverse is true for the second two sets, where either the shape or the dimensions are mismatched.

3.4   PuO$_2$ Experiment

Measurements were also made with plutonium oxide hemispherical shells at Lawrence Livermore National Laboratory. For these measurements, each hemispherical shell was taped to a 1.27 cm thick high density polyethylene (HDPE) shell with the same diameter

Object 1	Object 2	Feynman-Y	$P(\chi^2,NDF)$
Circle, 12.19 cm	Circle, 12.19 cm	-0.1472	0.7993
Circle, 16.26 cm	Circle, 16.26 cm	0.1060	0.0843
Circle, 20.32 cm	Circle, 20.32 cm	0.0808	0.1223
Circle, 24.38 cm	Circle, 24.38 cm	0.1642	0.0126
Circle, 28.45 cm	Circle, 28.45 cm	-0.0160	0.0161
Square, 16.26 cm	Square, 16.26 cm	0.1111	0.1263
Square, 20.32 cm	Square, 20.32 cm	-0.1531	0.3411
Circle, 16.26 cm	Square, 16.26 cm	0.2244	0.0006
Circle, 20.32 cm	Square, 20.32 cm	0.1987	0.0000
Circle, 12.19 cm	Circle, 16.26 cm	0.3237	0.0000
Circle, 12.19 cm	Circle, 20.32 cm	0.6086	0.0000
Circle, 12.19 cm	Circle, 24.38 cm	0.9249	0.0000
Circle, 12.19 cm	Circle, 28.45 cm	0.9227	0.0000
Circle, 12.19 cm	Square, 16.26 cm	0.4786	0.0000
Circle, 12.19 cm	Square, 20.32 cm	0.7044	0.0000

Table 3.1. Results from combining different sizes of circles (diameter) and squares (side length) traced out by a Cf-252 source. The top section contains matching objects, the middle section compares a circle with a square of approximately the same sieze, and the bottom section compares objects of different sizes.

and placed on opposite sides of the mask. The spheres were aligned so that the center of the sphere was 40 cm from the outer edge of the mask and vertically aligned with the center row of the mask. A laser pointer which cast a line beam was used to align the objects by holding it above the system so that the beam bisected the detector holder and each PuO_2 sphere.

Two Pu experiments are presented to demonstrate true positive and true negative measurements of distributed sources, i.e., one experiment with two identical items and one with two different items. These measurements were performed with plutonium dioxide (PuO_2) hemispherical shells at Lawrence Livermore National Laboratory. In the first experiment, the spheres were arranged with the PuO_2 hemispheres positioned on opposite sides of the mask, as shown in Fig. 3.7. This represents a true positive test case in which the two items should be identical. In the second experiment, one of the spheres was rotated by 90 degrees such that one hemisphere sat vertically and the other sat horizontally. This represents a true negative case in which the two items were different. These measurements will be referred to as the "true positive" and "true negative" tests, respectively. They were each taken for a little over 48 hrs and had 8661 and 8073 counts, respectively.

A measurement was also made with the plutonium shells together on one side of the mask, as a hollow sphere.

Fig. 3.8 shows the neutron count rates vs. mask rotation angle, Fig. 3.9 shows the distribution of count rates per unit angle, and Fig. 3.10 shows the reconstructed radiation images.

While the true positive case has an approximately constant count rate vs. mask rotation angle, the true negative case shows a modulation pattern in its count rate vs. mask rotation angle. The count rate distribution is more consistent with a Poisson-distributed random variable for the true positive case than the true negative case, which is quantified in the reduced χ^2 values shown in Table 3.2. The p-values associated with these measurements are consistent with the null hypothesis for the true positive case and inconsistent for the true negative case.

It is interesting to note that the reconstructed image of the true negative case (Fig. 3.10b) exhibits an excess below a vertical position of zero at about -50 degrees and above zero at about 130 degrees. This is consistent with expectations given that the horizontal hemispherical shell was at -50 degrees and had excess material on the lower half of the shell when compared with the vertically aligned hemispherical shell. Because there was no neutron emitting material on the upper half of the rotated item, the vertical item at 130 degrees presented excess material on the upper half of the item. That is, the reconstructed image indicates the difference between the two items, showing the shape of the material which did not match the object on the other side of the mask, a half-circle with a radius on the order of 5 cm. The positive case, as expected, does not show any strong region of neutron emitting material in its reconstructed image and is consistent with noise.

The measurements were run for 2 days each, but an analysis of the χ^2 value over time showed that the value converged in approximately 25 hours for the true positive case and 15 hours for the true negative case.

3.5 Conclusion

This chapter experimentally showed that the CONFIDANTE concept can be used to distinguish between matching and non-matching objects by measuring ^{252}Cf sources and PuO_2 hemispheres in several configurations. The ^{252}Cf sources were measured as a single source, as sources placed on exact opposite sides of the system, as sources placed on opposite sides of the system but misaligned by a small amount, and on a stage used to trace out squares and circles of multiple sizes. The single and matched point sources behaved exactly as expected. The smallest misalignments could not be identified using the Feynman-Y metric, but the 2.5° could. However, with a long measurement the difference was not as noticeable, which deserved further investigation. The shapes traced out by the stage performed as expected: measurements of matching objects were identified as matching and the non-matching objects were identified as non-matching.

Figure 3.7. CONFIDANTE with the LLNL PuO$_2$ hemispheres.
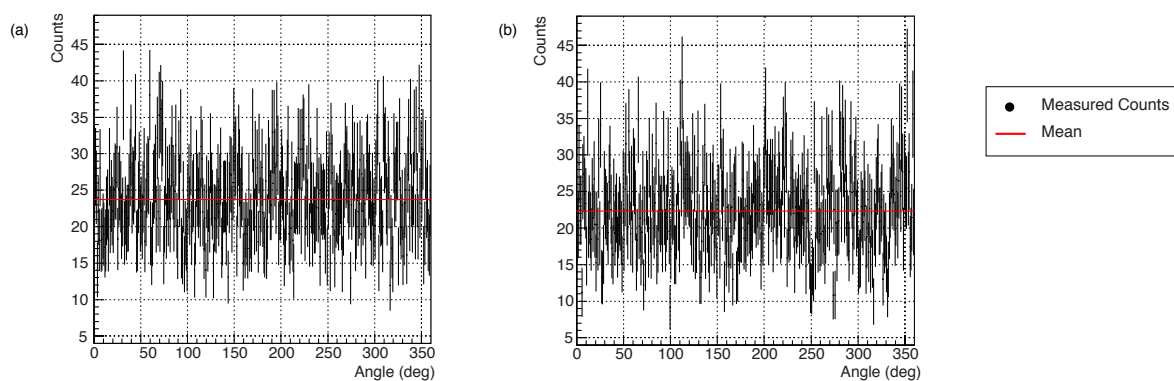
Figure 3.8. Count rate in the detector as a function of mask rotation angle for (a) Pu hemispheres aligned (b) one Pu hemisphere rotated by 90 degrees. The red line is the mean value of counts per angle.
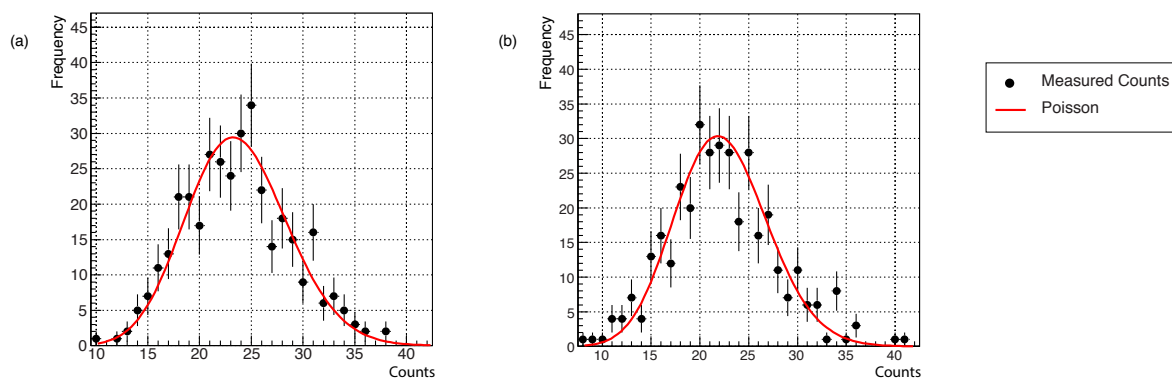
Figure 3.9. The distribution of counts per unit angle for (a) Pu hemispheres aligned (b) one Pu hemisphere rotated by 90 degrees. The red line is the expectation for a Poisson distributed variable with the same mean and integral value as the data.
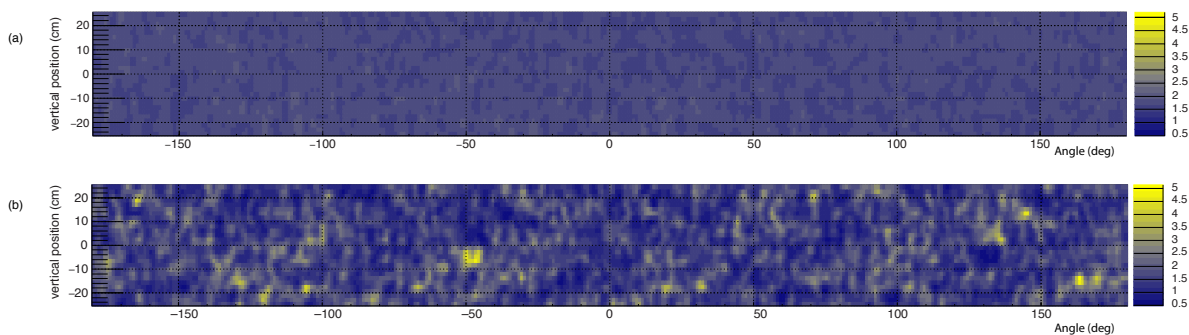
Figure 3.10. Image reconstruction using MLEM for (a) Pu hemispheres aligned (b) one Pu hemisphere rotated by 90 degrees.

The PuO_2 hemisphere results were as expected, with the most notable observation being that the reconstructed image of the hemispheres in non-matching positions reconstructed an approximate image of the difference between the two objects. This could put sensitive data at risk if images were reconstructed but there was some misalignment or mismatch between the tested objects. However, the image reconstruction is not necessary to evaluate if objects are similar; the analysis of the count rate variation is enough. Therefore future implementation should only test for consistency with a Poisson-distributed flat distribution without regard for the angular orientation of the mask. Only saving the histogram of count values in each angular bin without angular information from the data would remove the risk of revealing information about the geometry of the objects, even in the event of a false negative, such as misalignment of objects.

Table 3.2. Table of χ^2 results for selected Cf-252 and PuO$_2$ experiments. All tests have $\nu = 359$ degrees of freedom.

Source	Dwell Time (hrs)	Total Counts	χ^2/ν	p-value
Cf-252 single source	6.67	8597	5.12	0.000
Cf-252 single source with a 180° phase shift	6.67	8597	4.95	0.000
Cf-252, one source on each side of mask	3.33[1]	8738	1.03	0.3230
Rotated PuO$_2$ hemi-spheres on opposite sides	48.3	8073	1.29	0.0001
Matched PuO$_2$ hemi-spheres on opposite sides	48.3	8661	1.09	0.1220

[1] This was synthesized using two statistically indepedent measurements of a single Cf source, each 3.33 hrs long.

Chapter 4

Design Optimization

This chapter describes work done to improve the system design over the proof of feasibility system design using computer simulations. Following the feasiblity measurements, several potential improvements were identified. We used simulations to look at three types of changes relating to the shape, the size, and the rotation mode of the system.

We had noticed that there were imperfections in the modulation pattern caused by the shape of the mask. Ideally, the mask transitions sharply from letting radiation through an aperture to blocking radiation. That the mask is not completely opaque, that is, it lets through some radiation, does not change the ability to confirm similar objects as long as the background rate is small compared with the signal modulation of the mask. However, partial attenuation through the mask causes more variability than expected, which can cause issues. For example, the path of radiation from a source with a large vertical displacement relative to the detector would pass through multiple layers of the mask at an angle. See Fig. 4.1 for an example. One way to solve this issue is to make the mask spherical instead of cylindrical, so that all paths from a source to the detector are parallel to the mask elements, as shown in Fig. 4.2. A spherical detector and hexagonal mask elements were also proposed to match the spherical mask shape, though it was unclear if the benefits would outweight the detriments, especially in context of manufacturing difficulty.

We also wanted to know if we could make the system smaller so that it would be easier to move and potentially able to be set up closer to the measured objects, thereby increasing the signal. However, there are significant tradeoffs between the size of the system, imaging performance, and efficiency of a measurement. While CONFIDANTE does not require and, for security of data, should not produce images when implemented, it is a useful measure of the sensitivity of the mask to objects and features of different sizes. A mask or detector with smaller radius decreases efficiency and increases the measurement time or makes the angular resolution worse. Higher efficiency would increase the number of neutrons detected in a given dwell time but that requires a larger
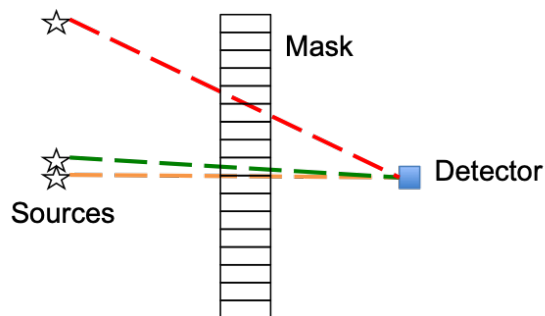
Figure 4.1. Drawing of cylindrical mask cross section with paths from sources to the detector, not to scale.
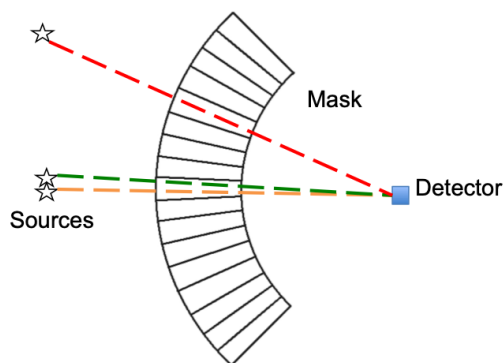
Figure 4.2. Drawing of spherical mask cross section with paths from sources to the detector, not to scale.

detector which worsens the angular resolution and performance unless the mask is proportionally increased in size as well. Imaging requires sufficient angular resolution to be sensitive to small features, but that either drives the system size up or the detector size down, decreasing efficiency and increasing measurement times. To that end, we looked at the effect of changing the outer diameter of the mask, the thickness of the mask, and size of the detector.

A perfect system and measurement would have as small a detector as possible, a thin but highly attenuating mask, and a high number of counts. Since there are limits on what attenuating materials exist and the length of time it is practical to take a measurement, trade offs must be made. We conducted a parametric study examining all of the factors previously discussed.

ROOT was used to simulate the mask and detector system using ray-tracing as described in Section 2.3.3. The sources were modeled using the detector response matrix to forward project the source term and produce an observation histogram. The metric for that response was calculated using either a reduced χ^2 or the likelihood metric

defined in the following section. Specific binning and count numbers are discussed in Sections 4.2 and 4.3.

4.1 Methodology

For some of the simulations, the Feynman-Y and χ^2 tests were used (see section 3.2.2). A new methodology was developed for others. The FY and χ^2 tests are good for testing a hypothesis but do not capture all the factors which are important for the tasks set for CONFIDANTE. Feynman-Y and χ^2 are quick to calculate, perhaps even possible for real-time updates during a measurement, but there is no upper bound for either. As a result, it functions well for evaluating a single measurement but less well when trying to compare a broad range and evaluate true positives and true negatives on an equal footing. For the mask and detector shape study described in section 4.2, the reduced χ^2 metric was suitable, but a new metric was designed for the extensive parametric studies on the size of the mask and detector. The new metric uses the Negative Log-Likelihood (NLL) value for a simulated measurement to calculate the predicted true positive or true negative rate. Its development was motivated by the need for a metric that was sensitive to the performance to confirm true positives (same objects) and true negatives (different objects) while incorporating the total detection efficiency of the system. In TEI systems it is especially true that the detection efficiency and the imaging performance are at odds, so they both need to be considered in the optimization.

NLL, like χ^2, is often used in fitting or iterative methods as a maximization metric (minimization in the case of χ^2).

The likelihood function for a sequence of independent observations X_n is equal to the product of their probability mass functions:

$$L(\lambda; x_1, ...x_n) = \prod_{j=1}^{n} f_X(x_j; \lambda) \tag{4.1}$$

The probability mass function for the Poisson distribution is:

$$p_X(x_j) = \begin{cases} \exp(-\lambda_0)\frac{1}{x_j!}\lambda_0^{x_j} & \text{if } x_j \in \mathbb{N}_0 \\ 0 & \text{otherwise} \end{cases} \tag{4.2}$$

So then the likelihood function for our set of observations from a Poisson distribution is:

$$L(\lambda; x_1, ...x_n) = \prod_{j=1}^{n} \exp(-\lambda)\frac{1}{x_j!}\lambda^{x_j} \tag{4.3}$$

Where j is taken over the $n = 300$ angular bins. In practice the negative log-likelihood function is much more commonly used so that the end result is a sum of positive numbers:

$$L(\lambda; x_1, ...x_n) = -n\lambda - \sum_{j=1}^{n} \ln(x_j!) + \ln \lambda \sum_{j=1}^{n} x_j \qquad (4.4)$$

For our purposes, we calculated the likelihood distribution for a constant rate (the ideal observation for perfectly matched objects), then the likelihood distribution for simulated data, and compared them. Since even the ideal case has Poisson-distributed noise, the "ideal likelihood" is actually a distribution, so the distributions for the ideal and simulated cases were calculated. Based on the ideal likelihood distribution, a threshold likelihood value was set at which 95 % of the "ideal" trials passed. If the simulated objects matched, then the likelihood values from the simulation would fall below the threshold, but would not if the simulated object were different.

For a given set of independent parameters, several simulations would be run, such as matching point sources, a point source and a larger ring source, and matching and non-matching ring sources at various diameters. For each simulated source configuration, the fraction of passing likelihood was calculated. For non-matching objects, the final reported value was one minus the fraction passing, so that a higher value always meant better performance for a simulation, whether matching or non-matching. For each set of parameters, the final metric was the sum of the likelihood threshold passing or not-passing value from all of the simulated source configurations.

The specific steps to calculate the likelihood metric are as follows:

First, calculate the likelihood distribution for the ideal case of a constant rate with Poisson-distributed noise.

1. Given N total counts and j mask rotation angle bins, the expected constant rate is the mean which equals $\frac{N}{j}$ counts.

2. Populate an observation histogram with random numbers from a Poisson-distribution with a mean of $\mu = \frac{N}{j}$.

3. Calculate the NLL for that observation histogram using Eq. 4.4

Repeat these steps to create the distribution of NLL values for the ideal case of a constant rate. For the calculations in this chapter, the steps were repeated 1000 times. Bin these values to create a histogram and fit a Gaussian distribution to the histogram. Calculate the threshold for 3σ (99.7 %) of the values, i.e. $\mu \pm 3\sigma$.

Second, calculate the likelihood distribution for each source distribution of interest. Using the detector response matrix, forward project the source term to generate an observation histogram with N total counts. Calculate NLL for that histogram using Eq. 4.4.

Repeat the first two steps to get the distribution of NLL values for that source configuration. For the calculations in this chapter, the steps were also repeated 1000 times.

The metric for the source configuration is calculated as the true positive or true negative rate depending on whether the source configuration had matching objects or different objects. For a source configuration with matching objects, the true positive rate is the fraction of NLL values which fall within the threshold calculated from the ideal constant rate. For a source configuration of non-matching objects, the true negative rate is the fraction of NLL values which are above the threshold.

Each system geometry was evaluated with several matching and non-matching source configurations. The final metric for a given geometry was the sum of all the true positive and true negative fractions. A higher metric indicates better performance from the system.

4.2 Mask and Detector Shape Simulations

The first set of simulations modeled combinations of three mask geometries and two detector geometries: a cylindrical mask with rectangular elements, a spherical mask with rectangular elements, and a spherical mask with hexagonal elements; each with both cylindrical and spherical detectors. The radius, thickness, and angular resolution of the mask as well as the mask pattern were kept identical for every simulation. The cylindrical mask with rectangular elements matched the proof of concept system with an inner radius of 44.92 cm, mask thickness of 10.16 cm, and 17 rows with 150 elements per row. The height of the spherical mask was calculated to be approximately the same angular field of view as the cylindrical mask, which was $40°$, and divided evenly into 17 rows. The detector was either a cylinder with a 2.54 cm diameter and 2.54 cm height or sphere with 2.54 cm diameter placed at a height aligned with the center of the mask height. Illustrations of the modeled mask geometries with a cylindrical detector are shown in Figure 4.3.

A single point source was modeled on each side of the mask (180 degrees apart), similar to the experimental configuration used in the proof of concept experiments. The first set of simulations used detector response matrices with a source space binned into 360 angular bins going from -180 to 180 degrees, 1 depth bin going from 100 to 101 cm, and 54 vertical bins going from -25.4 cm to 25.4 cm. Each simulation was run with 1.4 million neutrons for an average of 3800 neutrons per degree as the mask turned. A large number of neutrons was desired to see the effect of the equivalent of many hours of data. While no one measurement would collect that many neutrons, it both emphasized the differences between the mask responses and showed the potential effect of taking many measurements and saving the data from all of them. The height of the two sources was varied from -25 to $+25$ cm, with 0 being at the centerline of the mask, aligned with the
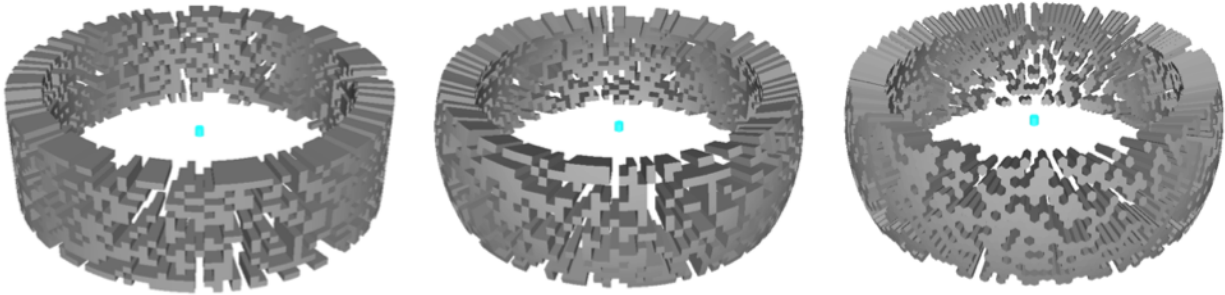
Figure 4.3. Examples of modeled mask geometry. From left to right, the cylindrical mask with rectangular elements, spherical mask with rectangular elements, and spherical mask with hexagonal elements. All are pictured with a cylindrical detector.

Mask Shape	Mask Element Shape	Detector Shape	Mean	Std. Dev
Cylindrical	Rectangular	Cylindrical	76.69	33.79
Spherical	Rectangular	Cylindrical	49.89	16.78
Spherical	Hexagonal	Cylindrical	50.57	15.24
Cylindrical	Rectangular	Spherical	76.79	36.23
Spherical	Rectangular	Spherical	46.16	16.29
Spherical	Hexagonal	Spherical	47.00	13.91

Table 4.1. Mean and standard deviation of the χ^2 values for each model.

detector. The imaging performance was calculated using a reduced χ^2 metric comparing the number of counts per angular bin with the mean number of counts per bin.

The results of the ROOT simulations are shown in Fig. 4.4 through Fig. 4.8. Simple linear and quadratic fits are included to guide the eye and emphasize the general trends: there are significant improvements from using a spherical mask but negligible differences from changing the mask element or detector shape. Figure 4.4 compares the results from a cylindrical mask and a spherical mask, both with rectangular mask elements and a cylindrical detector. The cylindrical mask exhibits significant deviations from the constant rate when the sources are positioned significantly above or below the detector as expected, which produces high reduced χ^2 values. The spherical mask does not exhibit this behavior; the reduced χ^2 values have some variation but exhibit no trends. Fig. 4.5 compares spherical masks with rectangular or hexagonal mask elements, both with a cylindrical detector. The spherical mask with hexagonal elements does not exhibit noticeably different performance than the spherical mask with rectangular elements. Comparisons of cylindrical and spherical detectors for each of the mask and mask element combinations are shown in Fig. 4.6, Fig. 4.7, and Fig. 4.8. The spherical
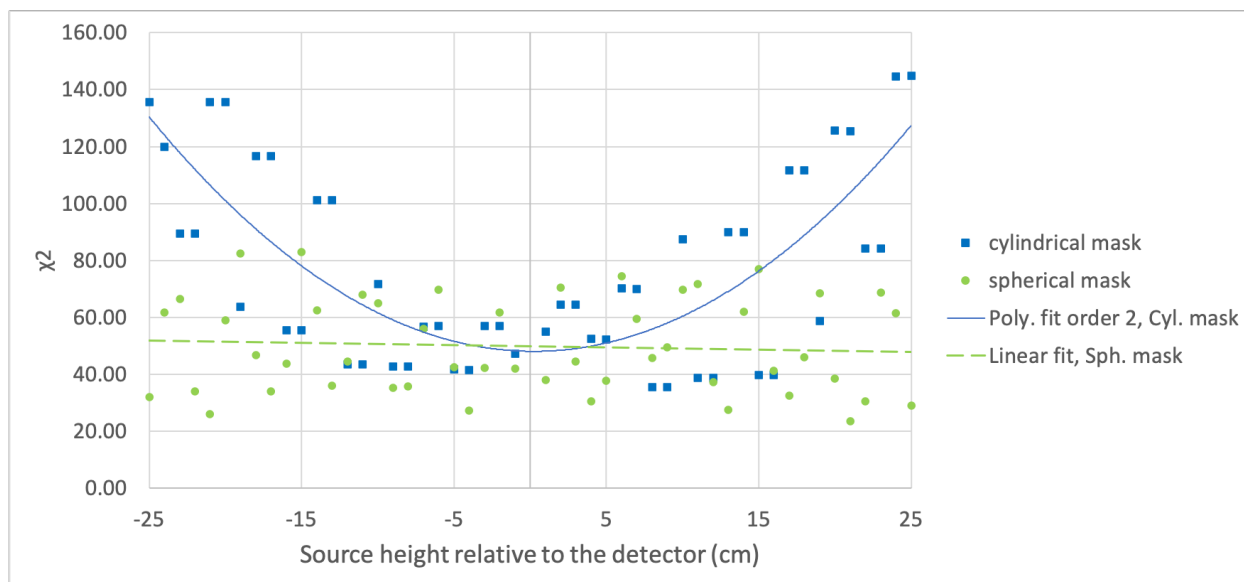
Figure 4.4. Comparison of χ^2 values for cylindrical and spherical masks with rectangular elements and a cylindrical detector.
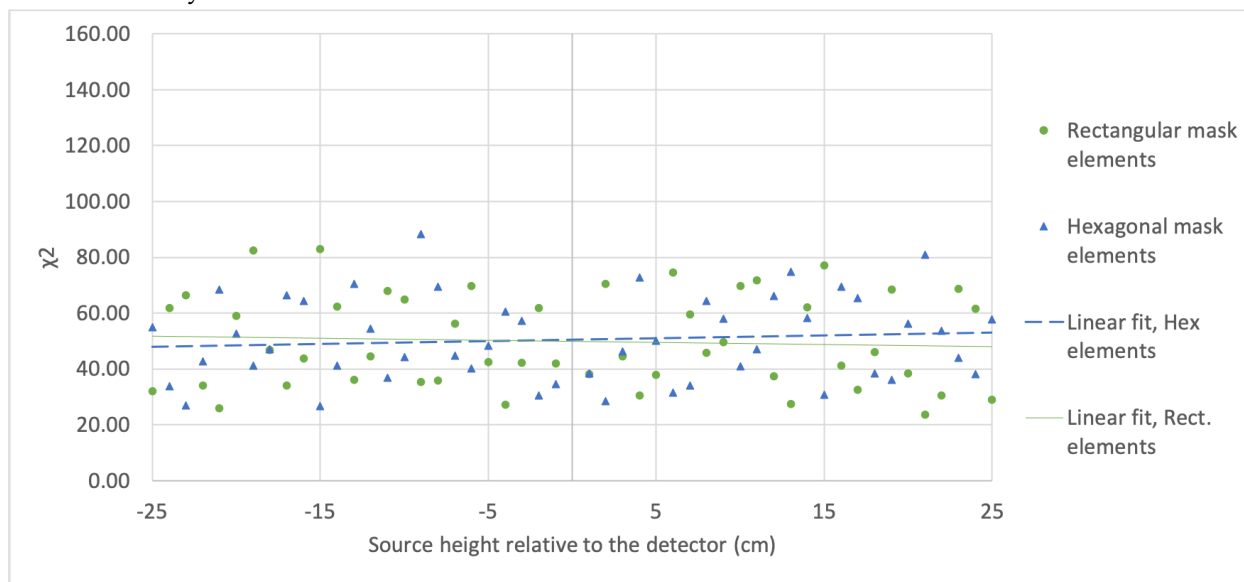
Figure 4.5. Comparison of χ^2 values for a spherical mask with rectangular or hexagonal mask elements and a cylindrical detector.
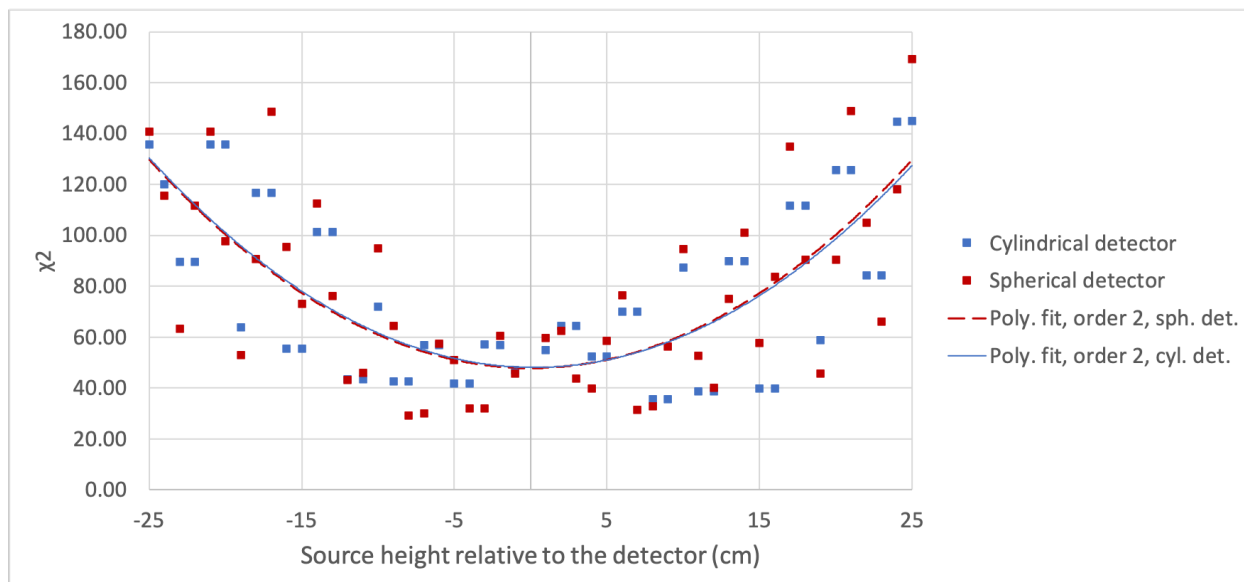
Figure 4.6. Comparison of χ^2 values for spherical and cylindrical detectors with a cylindrical mask with rectangular elements.
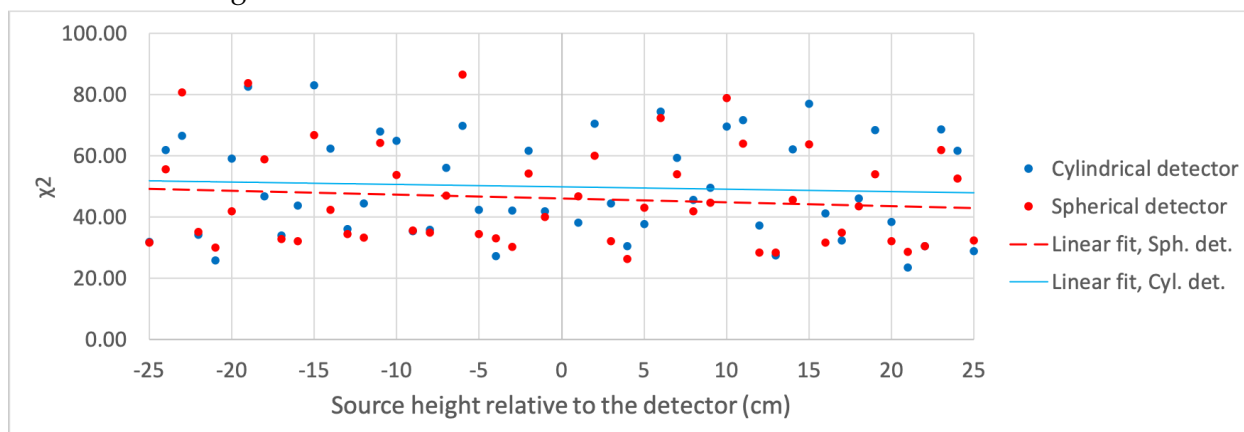
Figure 4.7. Comparison of χ^2 values for spherical and cylindrical detectors with a spherical mask with rectangular elements.
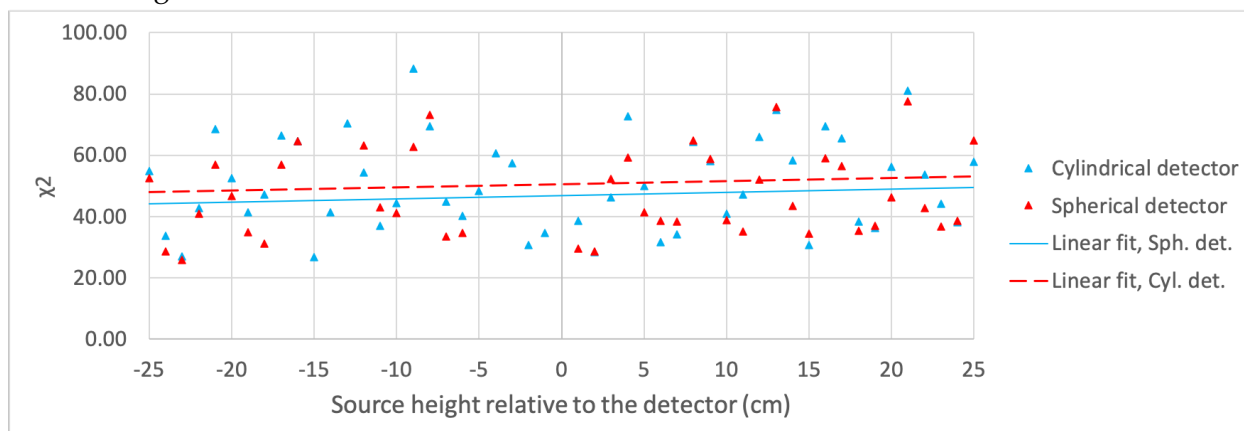
Figure 4.8. Comparison of χ^2 values for spherical and cylindrical detectors with a spherical mask with hexagonal elements.

detector results have a slightly lower mean than the cylindrical detectors, but much less than the standard deviation for either. Table 4.1 shows the mean and standard deviation of the χ^2 values for each simulation.

Based on these results, there is significant improvement in using a spherical mask instead of a cylindrical mask but negligible differences by switching to a spherical detector or hexagonal mask elements. Because of the difficulty in constructing either hexagonal elements or spherical detectors, we pursued a spherical mask with rectangular elements and a cylindrical detector.

4.3   Mask and Detector Size Simulations

The second set of simulations examined the size of the system. There were three independent parameters: mask thickness, detector diameter, and number of counts. All detectors were cylinders where the diameter and height were equal. Based on the previous section, all of the masks were spherical with rectangular mask elements. The same mask pattern was used for all masks. The number of counts was used as a proxy for length of time for a measurement. Specific values for real objects were not calculated, but 1×10^9 source neutrons emitted into 4π was chosen as an reasonable order of magnitude for reasonable source strengths and total measurement times after discussion with experts. Estimated values for the detector efficiency, transmission through the mask, and solid angle from the source to the detector were used to estimate the total number of detected counts for each of the mask-detector pairs.

That is:

$$\text{Total detected counts} = eff \times masktransmission \times solidanglefraction \qquad (4.5)$$

The detector efficiency was calculated using:

$$eff = 1 - .9^{(d/2.54)} \qquad (4.6)$$

Where d is the diameter of the detector in centimeters, assuming a cylindrical detector.

The transmission factor through the mask is the 50 % open fraction plus the transmission through the mask thickness:

$$masktransmission = 0.5(1 + \exp \frac{-t}{4}) \qquad (4.7)$$

Where t is the thickness of the mask.

The solid angle fraction of 4π of the detector from the source was calculated as:

$$solidanglefraction = 0.5 \times (1 - \cos(\arctan(d/2/l))) \qquad (4.8)$$

where d is the detector diameter and l is the distance from the detector to the source.

Additionally, a constant count rate of 20 % strength was added based on estimates of the baseline seen in measurements.

The parameters for the set of simulations were:

Emitted source neutrons	1×10^9
Outer diameter (cm)	38.1 cm
Mask Thickness (cm)	0.5, 2.5, 5.0, 7.5, 10.0
Detector diameter/height (cm)	2.54, 3.81, 5.08
Sources	point,5 cm, 10 cm, 15 cm, 20 cm, 25 cm diameter rings

For the likelihood simulations, the detector response matrices were changed to be spherical to match the mask. The source space had 300 angular bins in ϕ from $-180°$ to $180°$, 34 angular bins in θ from $70°$ to $110°$, and one depth bin from 100 cm to 101 cm. The NLL calculation was repeated 10^4 times to build the likelihood distributions.

The immediate conclusion from the sum of the likelihood metric calculations, shown in Table 4.2, is that a thicker mask and a larger detector is better. Breaking the metric down by whether the objects were matching or not allows more insight in the some of the tradeoffs. It is also important to look at the separate results as there were more non-matching source configurations than matching source configurations, but the relative importance of the tests was not represented in the total metric. The sums of the likelihood metrics for just the matching object simulations is shown in Table 4.3 and the sums for dissimilar objects in Table 4.4. Notably, the sums for the like objects are much

		Mask thickness (cm)			
		2.5	5	7.5	10
Detector height/diameter (cm)	2.54	6.9192	11.1604	12.803	13.8099
	3.81	9.8628	14.1642	15.7638	16.4868
	5.08	11.4244	15.4593	16.9132	17.5244

Table 4.2. The likelihood metric results from simulations with different mask thicknesses (the columns) and detector diameter/height (rows).

		Mask thickness (cm)			
		2.5	5	7.5	10
Detector height/diameter (cm)	2.54	5.9006	5.2221	5.0021	4.9843
	3.81	5.6506	4.9867	4.981	4.9686
	5.08	5.4846	4.9847	4.9647	4.9176

Table 4.3. The likelihood metric sum for matching objects. There were six sets of matching objects, so the maximum possible metric is six.

Detector height/diameter (cm)	Mask thickness (cm)			
	2.5	5	7.5	10
2.54	1.0186	5.9383	7.8009	8.8256
3.81	4.2122	9.1775	10.7828	11.5182
5.08	5.9398	10.4746	11.9485	12.6068

Table 4.4. The likelihood metric sum for combinations of two dissimilar objects. There were 6 different objects simulated, for a total of 15 objects and maximum possible sum of 15.

more tightly clustered, while there is a much larger spread in the sums of the dissimilar objects. This emphasizes the importance of the modulation for distinguishing objects. These results also address the concern that a thick mask and large detector would cause deviations from a Poisson distribution because the detector could be larger than the projection of a single aperture and particles pass through a portion of a mask element instead of the full amount. The larger detector does have a lower metric for similar objects, but the difference is fairly small, especially for the thick masks. This improvement is probably caused by the increased efficiency in a larger detector.

Based on this study, the best performance was from the largest detector and thickest mask, which were the 5.08 cm diameter detector and the 10 cm thick mask. The complete array of results from this parametric study is in Appendix A

4.4   Conclusion

This chapter presented the results from two sets of simulations and explained the new methodology developed to evaluate system designs. The methodology uses NLL to calculate true positive and true negative rates for source configurations of matching and non-matching objects. This means the metric measures the sensitivity of the system to different feature sizes and can be used to optimize a system for the tasks we defined. While these simulations took a parametric approach, this methodology can be extended to optimize the system for specific models or features.

Based on these simulations, the best system has a thick spherical mask with rectangular elements and a cylindrical detector. While the spherical detector performed a little bit better than the cylindrical detector, it is important to remember that the simulation was an idealized sphere, and in reality constructing a spherical detector would be difficult to make and not be as efficient as the simulation. While an interesting concept, it was not pursued any further.

There was not a clear optimal size. An even larger and thicker mask would probably perform better if the outer radius constraint was removed, but given the practical constraint of how close a measurement can be made to relevant items, the larger mask

would cause the source to eventually be placed futher away. The $\frac{1}{r^2}$ effect would make the measurement less efficient as well as making the item smaller angularly. Within these constraints, this system geometry is reasonably optimized.

The next chapter describes the fabrication of a spherical mask and compares its performance with these simulations and the first system.

Chapter 5

Demonstration System

Based on the simulations in Ch. 4, an improved system was built with a 3D-printed spherical mask. This chapter describes the fabrication and design as well as some measurements used to compare the new system with the simulations and previous system.

5.1 System description

Based on the studies described in Chapter 4, a spherical mask design with rectangular elements was chosen for the second mask design. The mask thickness was kept at 10.16 cm based on the studies. The mask pattern was not changed, i.e. there are 17 rows and 150 elements per row with the same pattern of apertures and mask elements. Future studies are needed to optimize the number of elements and the pattern of the mask. The following sections detail the fabrication of the mask using 3D-printing, including the choices of 3D-printing materials, and the rest of the system hardware.

5.1.1 Fabrication using 3D-Printing

Due to the spherical shape, the mask for this system could not be fashioned out of sheets of HDPE as the cylindrical mask was. Instead, it was 3D-printed. Two materials were considered for printing due to availability and cost: acrylonitrile butadiene styrene (ABS) and polycarbonate. Polycarbonate has a higher median density than ABS, 1.2 g/cc and 1.07 g/cc respectively, but ABS has a higher density of hydrogen atoms, which is the most effective attenuation material for neutrons [58]. The chemical formula for ABS is $(C_8H_8)x \cdot (C_4H_6)y \cdot (C_3H_3N)_z$). Polycarbonates have a chemical formula of $C_{16}H_{14}O_3$. It was not obvious whether the higher overall material density or higher hydrogen density would be a better mask material. For this application, it is not merely the attenuation length that matters but the scattering length; neutrons do not need to be captured in the

Material	Count rate (ns)
None	0.43 ± 0.015
HDPE	0.09 ± 0.0071
Polycarbonate	0.10 ± 0.0075
ABS	0.1161 ± 0.0080

Table 5.1. Table of neutron count rates with 10.16 cm plastic cubes between the Cf-252 source and detector. The ABS and polycarbonate blocks were 3D-printed at 100% infill.

mask but could scatter away from the detector or lose enough energy through scatter that their energy is below the energy threshold of the detector.

To decide between the different materials, we conducted some simple measurements to compare their effectiveness at modulating the detected rate of neutrons in the detector. A Cf-252 source was placed approximately 1 m from the detector with a block of plastic centered at 0.5 m from the detector, similar to the experimental setup of the CONFIDANTE system. Measurements were taken with no material, HDPE, ABS, and polycarbonate. The ABS and polycarbonate blocks were 3D-printed using fused deposition modeling (FDM) at 100% infill. The HDPE block was fashioned from the same sheets of HDPE from which the original mask was constructed. All plastic blocks were 10.16 cm by 10.16 cm by 10.16 cm cubes. Data was collected for 30 min for each block. Results are shown in Table 5.1.

Based on these measurements, polycarbonate was more effective than ABS at reducing the neutron count rate in the detector for a geometry similar to the proposed prototype geometry, so that was the material chosen for the mask.

The mask was printed in 10 pieces due to the size of available 3D printers. As shown in Fig. 5.1, small insets shaped like bowties were designed to lock the pieces together and prevent gaps between the pieces. Fig. 5.2 was taken when the mask was half-assembled, providing an excellent view of the inside and cross-section of the mask. It would be possible to print the mask in one piece but requires a printer with a printbed at least 76.2 cm by 76.2 cm by 40 cm. Like the test pieces, all mask pieces were printed at 100% infill.

5.1.2 System Hardware

The frame upon which the mask sits also holds the detector and electronics and was designed to make future upgrades and alignment during experiments easier. The top of the frame has a holder for a detector in the center and a platform for the mask. The platform is connected to a Teknic ClearPath servo motor (CPM-SCSK-3441S-ELNA) and rotates separately from the rest of the frame. The motor has an achievable resolution of 0.057 degrees and repeatability of 0.03 degrees. Combined with a worm gear speed

reducer (Boston Gear series 700), the motor encoder rotates 325800 steps to complete a 360-degree rotation of the mask.

The mask and platform have indents and pins on the base which connect to ensure consistent and secure placement of the mask on the frame. If a mask with a new pattern or material is desired, it will be easy to switch out. Fig. 5.1 is an overhead view of the mask on the platform without the detector. The detector sits in the middle, passing through the hole in the platform and aligned with the center of the mask using a custom holder attaching the detector to the frame. Fig. 5.3 shows a side view of the mask on the frame. The frame sits on a scissor-lift cart so that the field-of-view may be adjusted to center on the objects of interest. If test objects are in large containers or otherwise higher off the ground, it may be easier to adjust the system height than test object height.

The initial setup of the system used the same detector as the first system, a 2.54 cm by 2.54 cm cylindrical stilbene crystal coupled to a Hamamatsu 6094 PMT. The detector was read out using a CAEN DT5730 desktop waveform digitizer. Additional experiments are planned using 3.81 cm and 5.08 cm stilbene detectors coupled to Hamamatsu SiPM arrays coupled to custom summing boards.

Both the motor and digitizer are controlled with custom software over USB.

5.1.3 System calibration

The energy of the detector was calibrated with the Compton pulse height spectra from a ^{22}Na source and an ^{137}Cs source. Fig. 5.4 and Fig. 5.5 show the calibrated spectra.

The PSD calibration was done using a 252Cf source with the charge integration method described in Section 2.2.4. The optimized tail window started at 35 samples. The figure-of-merit calculated with Eq. 2.6 is shown in Fig. 5.7.

5.2 Measurements

A set of measurements were performed to evaluate the performance of the newly built system and benchmark it against the simulations and previous system. These were done with with a ^{252}Cf source. The matching sources used in Ch. 3 were quite weak, so a newer pair of matched sources was used, each 13.99 MBq. The source capsules measured 6 mm by 25 mm, but as before the material in the capsule was much smaller and approximated a point source. Using the stronger source decreased the time needed to get a high number of counts needed to reduce statistical uncertainties.

In many cases, the measurements had more counts than the simulations, which calculated counts in the detector based on a source strength of 1×10^9 neutrons and estimated efficiency for the detector and mask. Multiple independent data sets were measured for each source configuration, but even the shorter data sets had more counts than the sim-

Figure 5.1. A photo of the 3D-printed mask from overhead. Small 3D-printed wedges (in black) fit into the top surfaces of 10 arc segments of the mask to keep them locked together.

ulations. The mask was operated by rotating to discrete positions and collecting data for a dwell time of between 10 to 30 seconds. Because of the large collected statistics, we opted to use the observation histograms as distributions from which to randomly fill histograms for comparison, rather than try and scale the histograms by a constant fraction.

The following sections present two sets of measurements: first, a comparison of the spherical and cylindrical mask; second, an evaluation using matching and non-matching point and ring source configurations. Both are compared with the simulations from Chapter 4.
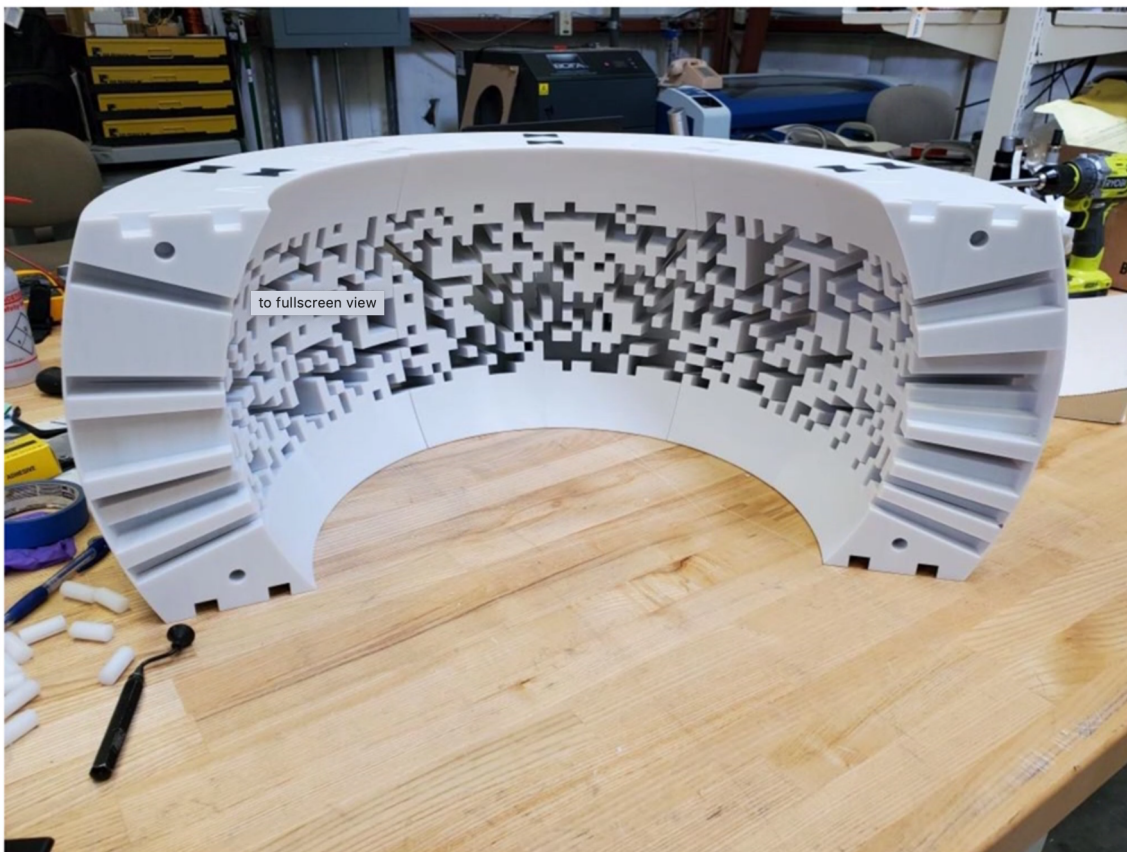
Figure 5.2. A photo of the 3D-printed mask half-assembled showing the cutaway side view.

5.2.1 Spherical-Cylindrical Comparison

Two measurements were taken to confirm the predicted improved performance of the spherical mask over the cylindrical mask as explained in Section 4.2. The sources were placed at a stationary location, both at the same vertical height as the detector as the detector in one measurement, and with a 28 cm vertical offset in the second measurement. These two measurements were done with both the first cylindrical and second spherical systems. Both masks have a field of view of approximately $\pm 20°$ and 28 cm is $15.64°$ above the centerline. Each measurement was done for approximately 5 hours which had approximately 200 000 counts total. The simulated observation histograms had only 13959 detected counts. Histograms of 14,000 counts were generated from these high statistics measurements so that they had the same statistical uncertainties.

Fig. 5.8 shows the results of the point measurements at different heights to compare

Figure 5.3. A photo of the 3D-printed mask installed on the system. It sits on a circular platform on top of a rectangular frame. The motor is mounted under the top of the frame and connected to the circular platform.

mask shapes. Linear fit lines are included to help guide the eye. The cylindrical mask reduced χ^2 value increased from 1.33 to 2.39 when the source was moved from in line with the detector to the elevated position. For the spherical mask, the values obtained from measured data were 1.08 and 1.06. The measured values for the cylindrical mask line up extremely well with the values from the simulation; the measured values for the spherical mask are actually much better than in simulation, that is, the reduced χ^2 is closer to one. It is clear that the spherical mask does much better than the cylindrical: the reduced χ^2 values are both lower and more consistent for the spherical mask, while the value is much larger for the elevated point source for the cylindrical mask.

Fig. 5.9 shows the modulation pattern from the measurements with the source in the elevated position. Although it is difficult to tell by eye, the modulation from the cylindrical mask has much more variation than the modulation from the spherical mask,

Figure 5.4. The measured pulse height spectrum using a ^{137}Cs source.
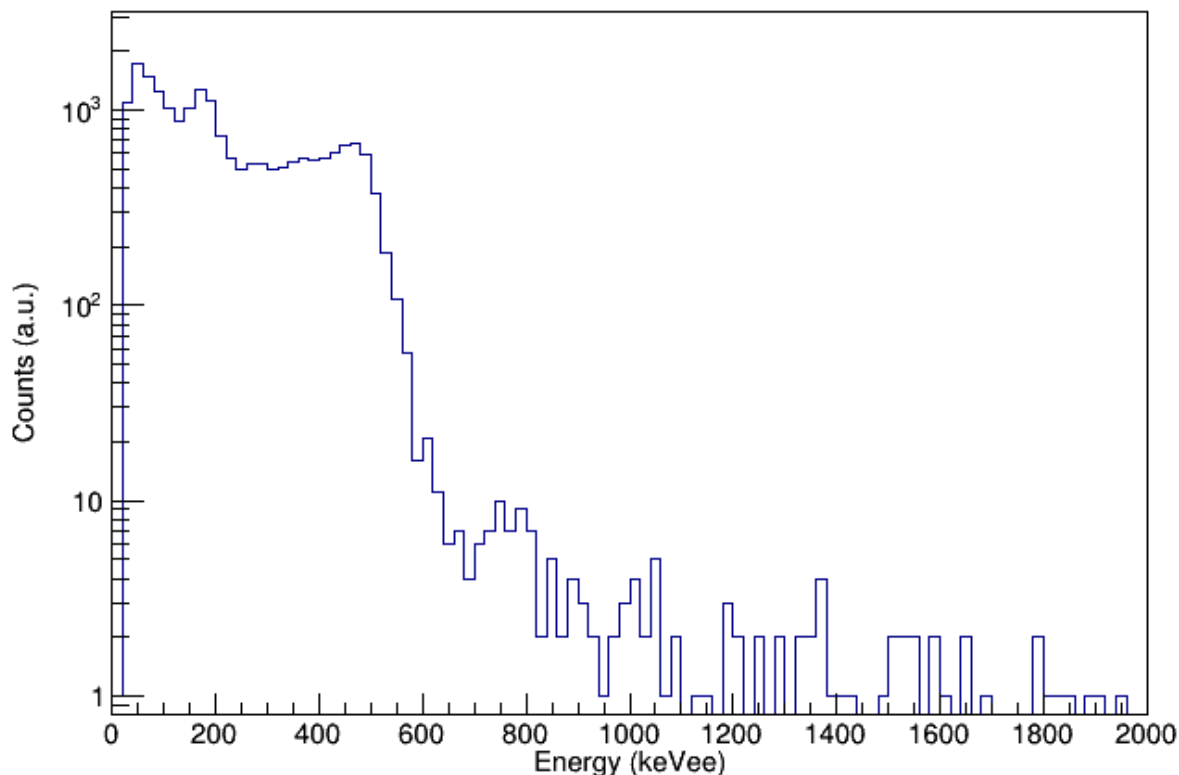
with the reduced χ^2 values of 2.39 and 1.06 respectively. The effect is more exaggerated with more counts; Fig. 5.10 shows the results if the measured data has 140 000 counts, ten times the previous amount. Although no single measurement would likely gather this much information, it shows the variation that might be expected if the data from several measurements were added together. With that much data, the respective reduced χ^2 values for cylindrical and spherical systems are 14.7 and 1.9, respectively. This extreme difference indicates the superiority of the spherical design in fixing the problem of paths from the source to the detector that are only partially attenuated instead of going through the full thickness of the mask.

5.2.2 Likelihood Comparison

The second set of measurements was done to investigate how well the new mask performed in distinguishing between different objects and matching similar objects using the same likelihood metric and methodology as developed in Section 4.3. In addition to
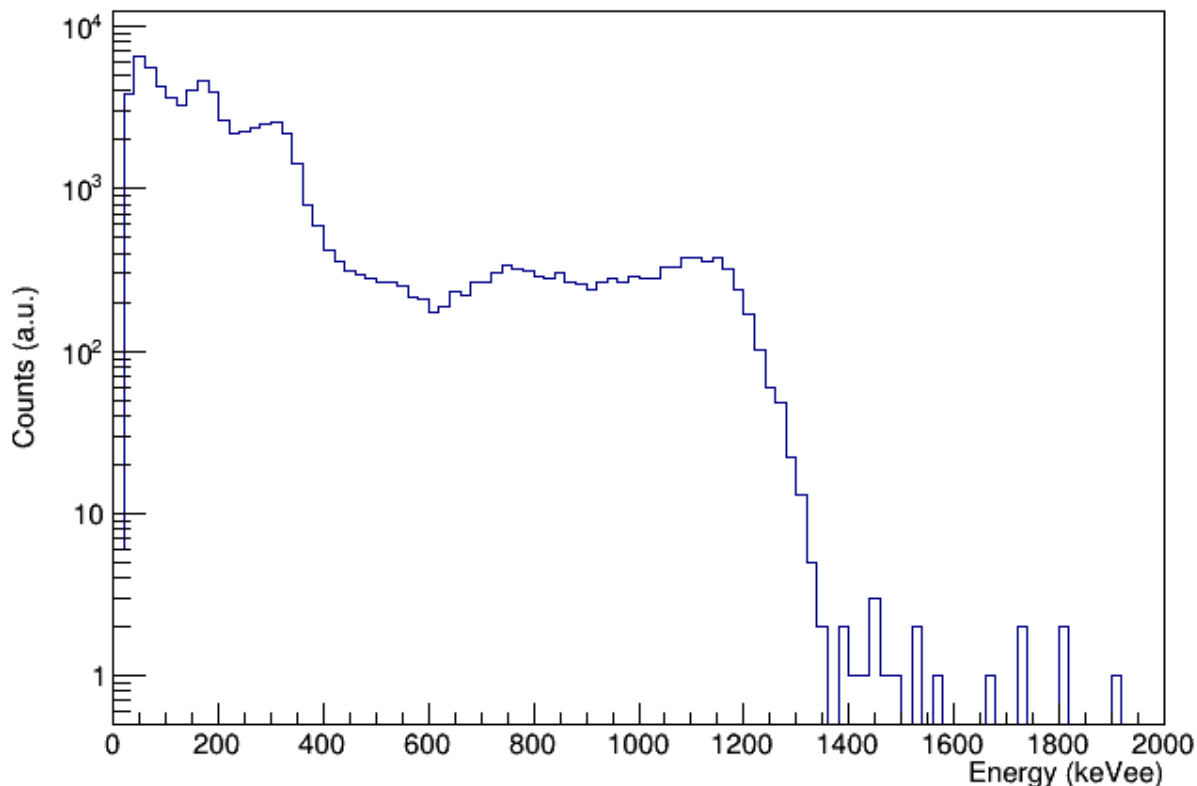
Figure 5.5. The measured pulse height spectrum using a ^{22}Na source.

point source geometries, the ^{252}Cf sources were placed on a vertically rotating stage to create rings with a diameter of 10 cm, 15 cm, 20 cm and 30 cm. Pairs of data sets were combined with a phase shift of 180° added to one set, as if it were placed on the opposite side of the mask from the other object. This removes error that might be involved with aligning two objects. Further testing with objects opposite each other is necessary.

Table 5.2 shows the likelihood metric results from pairing two data sets with a 180° phase shift added to one data set. The likelihood metrics result for the simulation with the same mask thickness and detector size are shown in Table 5.3 for easy comparison. All the listed values are the true positive fractions as described in Section 4.1. For matching objects, on the diagonal, a good value is close to 1.0, indicating data mostly flat with some noise. Off the diagonal, a good value is close to 0.0 because that indicates the differences in non-matching objects was detected. The color is intended to help indicate the better values, where green is good and yellow is less good.

Overall the system performed very well for matching objects, with over 0.99 true positive fraction for all combinations. For the non-matching objects, these results provide
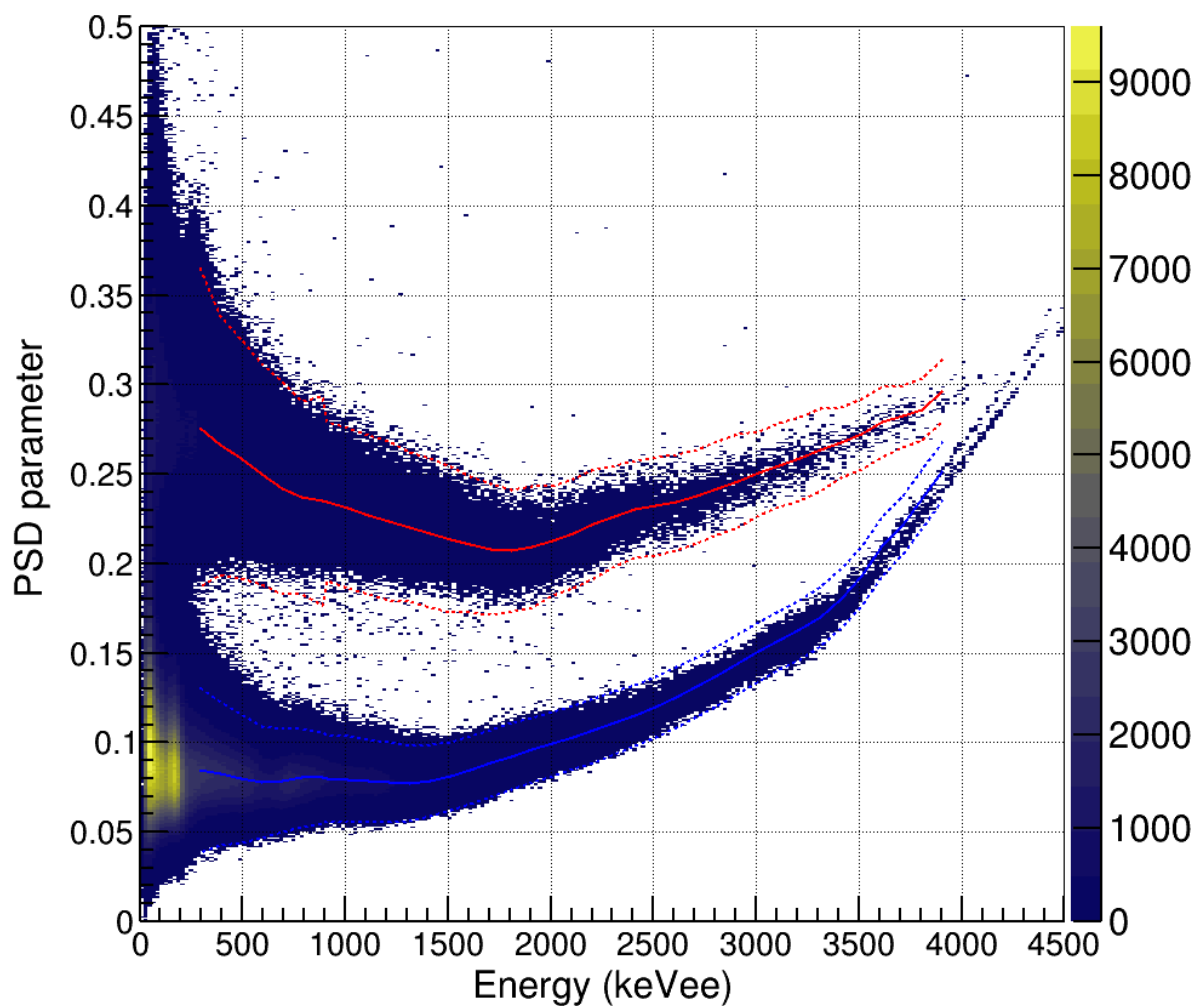
Figure 5.6. The measured pulse shape parameter vs. energy for the stilbene crystal. Neutron events lie within the upper band defined by the red dotted lines (the solid red line is the mean and dotted red lines contain 3σ deviations from the mean) while gamma ray events fall in the lower band defined by the blue dotted lines (the solid blue line is the mean and the dotted blue lines contain 3σ deviations from the mean).
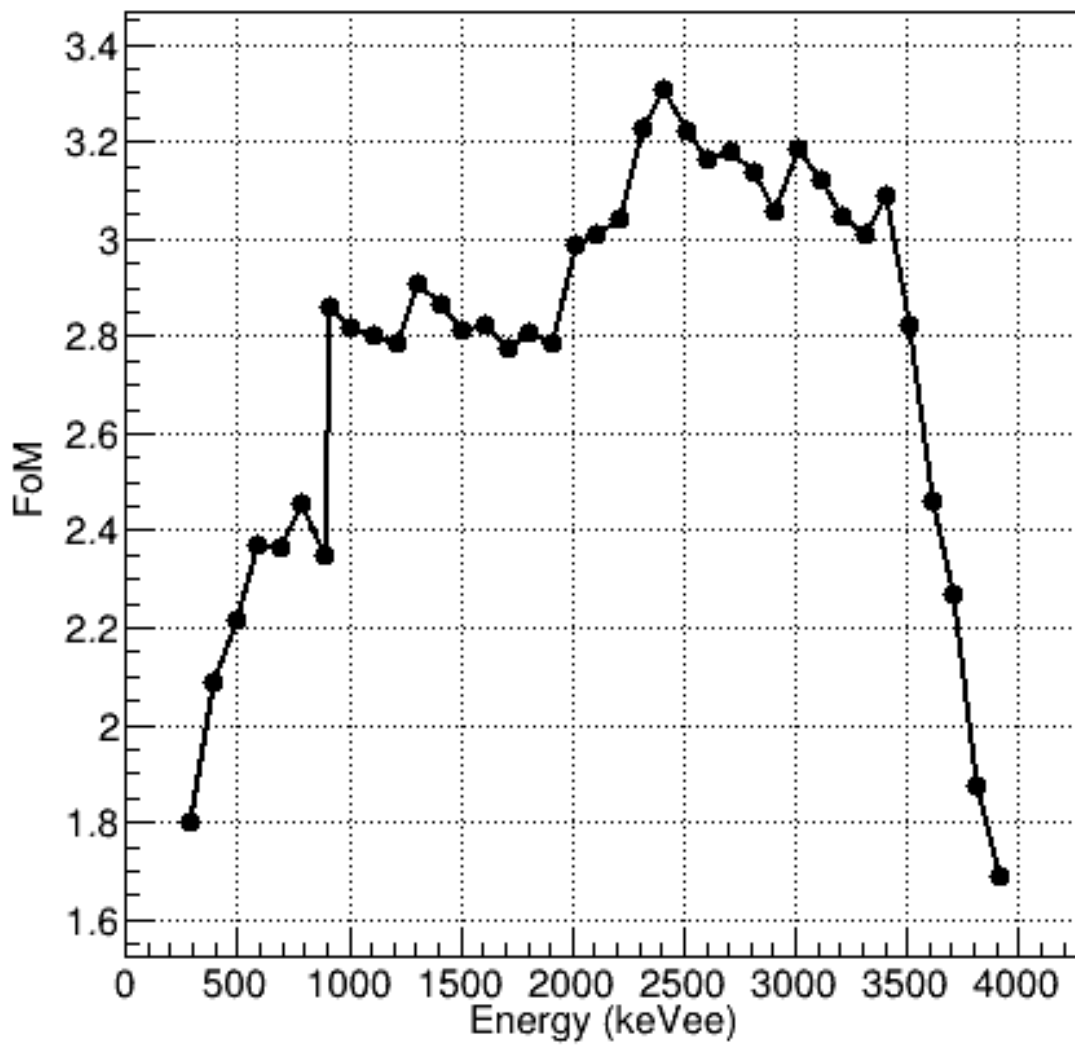
Figure 5.7. The figure-of-merit (FoM) as a function of energy for the stilbene crystal with a tail window starting 35 samples after the start fo the pulse.
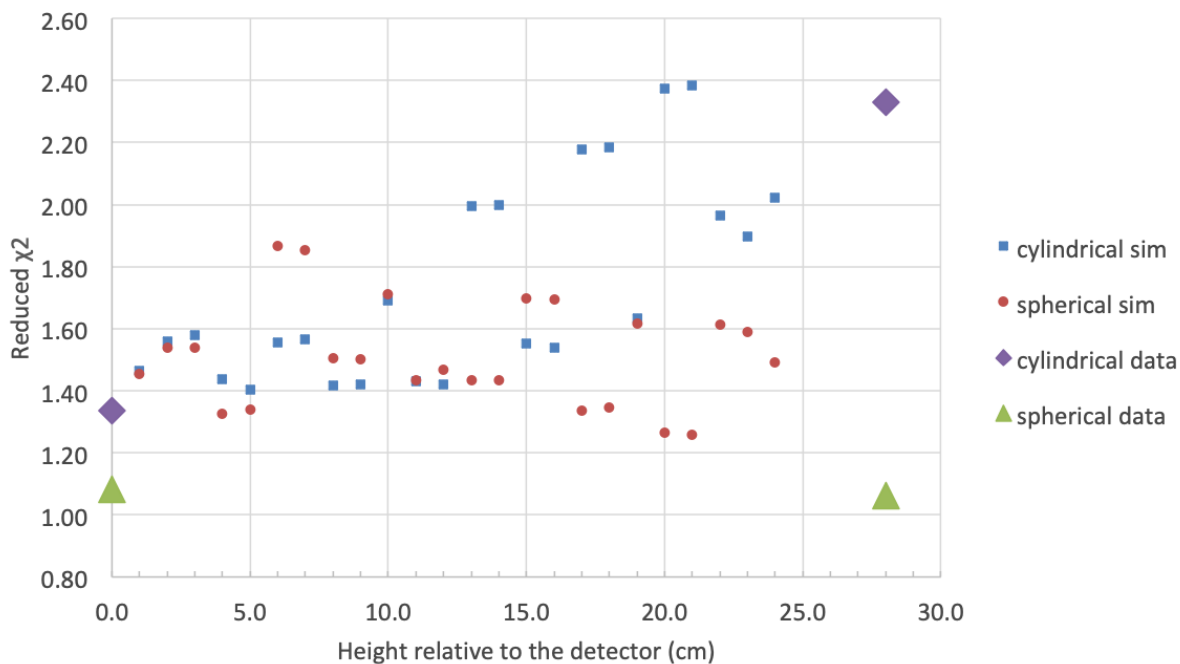
Figure 5.8. Comparison of mask shape simulations and data using the reduced χ^2 values for point sources either in line with the detector or elevated compared with the detector.
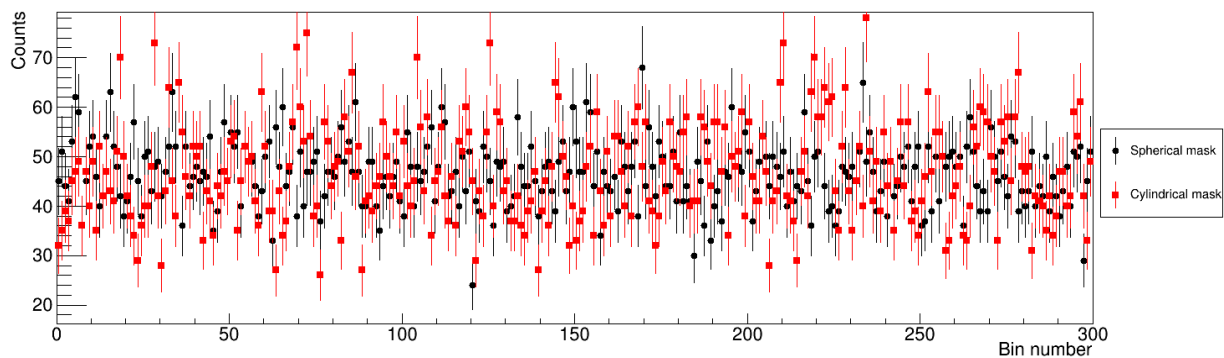
Figure 5.9. Comparison of the modulation patterns for a point source elevated 28 cm, approximated 15.6°, above the detector in the spherical (black) and cylindrical (red) systems. Each histogram has 14 000 counts total.
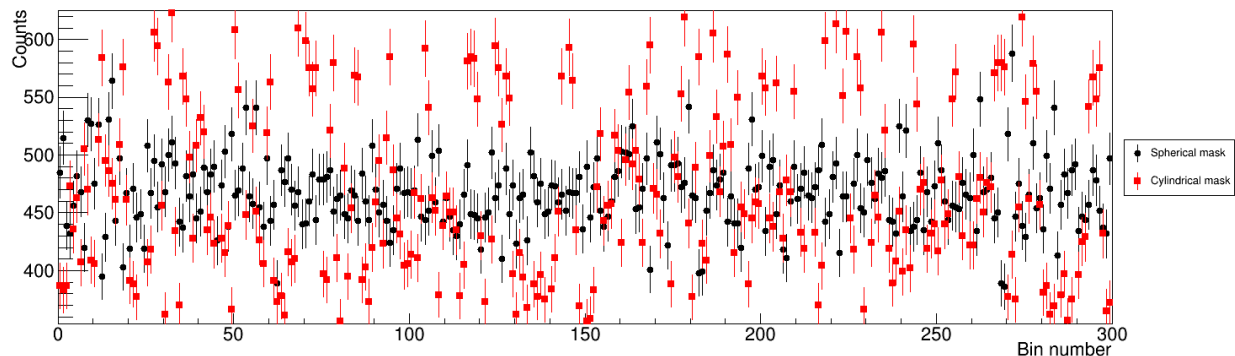
Figure 5.10. Comparison of the modulation patterns for a point source elevated 28 cm, approximated 15.6°, above the detector in the spherical (black) and cylindrical (red) systems. Each histogram has 140 000 counts total.

	pt	5cm	10 cm	15 cm	20 cm	25 cm
pt	0.995	0.287	0.518	0.293	0.135	0.0474
5 cm		0.996	0.904	0.66	0.312	0.352
10 cm			0.9898	0.926	0.7643	0.7266
15 cm				0.9901	0.9627	0.9291
20 cm					0.9964	0.9771
25 cm						0.9929

Table 5.2. Table of likelihood values for pairs of objects (indicated by row and column). The data from one object was shifted by 180 degrees in analysis and added to the data from the other object. For matching objects, on the diagonal, a good value is close to 1.0, indicating data mostly flat with some noise. Off the diagonal, a good value is close to 0.0 because that indicates the differences in non-matching objects was detected. The color is intended to help indicate the better values, where green is good and yellow is bad.

some understanding of the sensitivity of the system to different feature sizes and could be used as a reference if a specific size or difference in feature sizes is of interest. It is interesting to note that the true negative fraction is better for small differences in small features, that is, a 5 cm difference has a higher true negative fraction for the 5 cm and 10 cm objects than for the 25 cm object.

5.3 Conclusion

3D-printing the mask worked extremely well as a method for creating an unusual shape that would have been difficult to construct using conventional subtractive machining.

The spherical mask shows definite improvement in the response for sources placed toward the edge of the field of view. The reduced χ^2 values were fairly consistent for

	pt	5cm	10 cm	15 cm	20 cm	25 cm
pt	0.0008	0.5744	0.0288	0	0	0
5 cm		0.996	0.6769	0.0337	0.0001	0
10 cm			0.9973	0.9781	0.7199	0.2638
15 cm				0.9962	0.9881	0.9179
20 cm					0.9964	0.9927
25 cm						0.9976

Table 5.3. Table of likelihood values for pairs of objects (indicated by row and column) from simulation of a 10 cm thick spherical mask and a cylindrical detector with height and diameter of 2.54 cm. For matching objects, on the diagonal, a good value is close to 1.0, indicating data mostly flat with some noise. Off the diagonal, a good value is close to 0.0 because that indicates the differences in non-matching objects was detected. The color is intended to help indicate the better values, where green is good and yellow is bad.

the spherical mask, 1.08 and 1.06, while for the cylindrical mask it increased from 1.34 to 2.39. This will decrease the false negatives that could have been produced by objects off-axis from the detector in the cylindrical system.

The likelihood metrics in the data shows similar trends as the metrics from simulation. The metric is significantly better for the measured data than simulation for matching point sources. It is difficult to distinguish between objects that differ in diameter by only 5 cm, which is not surprising since the angular width of a single mask element is 2.4°, which is a width of 4.2 cm at the distance the source was placed. That said, while the true negative rates were as low as a few percent, the true positive rates were all above 0.989. There may need to be policy weigh-in to set an operating point on the positive/negative rates, but these results show that it is possible to separate them.

Additional experiments which would be useful include testing other detector sizes, as the simulation showed that the efficiency made up for worse imaging expected from a larger size. Stilbene detectors with height and diameter of 3.81 cm and 5.08 cm were ordered but experimental time was limited due to the pandemic.

Chapter 6

Conclusions and Future Work

The work presented in this dissertation was the start of developing CONFIDANTE for use in potential future arms control verification. A future arms control treaty may expand beyond nuclear warheads on deployed delivery systems and include tasks like counting inactive warheads or confirming warheads as part of a dismantlement procedure. New verification technology must be developed to address the sometimes conflicting needs of giving the inspecting party confidence to confirm declarations and assuring the host party that sensitive information about the declared items is protected and not at risk of being released. Many verification systems under development measured sensitive information and kept it secure behind an information barrier, but this poses some challenges for a monitor who must trust the final yes/no determination from the system without seeing any data. The most recent approach has taken the idea of Zero-Knowledge Proof (ZKP) from cryptography and applied the concept to warhead verification. In interactive ZKP, a prover demonstrates that they know a particular piece of information without revealing what it is by solving a challenge problem that can only be solved by someone who knows the secret information. In a warhead verification ZKP, the host country has declared that items are warheads and the inspector verifies this claim with a measurement whose result is consistent if and only if the host's declaration was true.

Advanced concepts in radiation detection and imaging made a fast neutron time-encoded imager a potential solution. The availability of PSD stilbene meant that we could separate the distinctive signatures of gamma rays and fast neutrons; this thesis focused on fast neutron applications, but the concept easily extends to gamma rays. Our ZKP approach used Time-Encoded Imaging (TEI) which meant the system was sensitive to the two-dimensional distribution of radioactive material of the items being measured, but by using an anti-symmetric mask, the two-dimensional image was only noise and contained no imaging information about the objects if and only if items being measured had matching distributions of radioactive material. Although the system does

reveal the total neutron count rate, which may contain some sensitive information, much less information cna be derived from neutron count rates than many other radiation measurements. It is possible that a party might share this as a provision of a treaty. If so, then the measurement data could potentially be viewed by the inspector while the measurement was being performed as well as viewing all the data at the end of the measurement. This would increase the inspector's confidence in the confirmation of the items while protecting the sensitive information for the host.

The following sections summarize the measurements and simulations done in the course of this thesis and present opportunities for future work.

6.1   Summary

This dissertation presented the feasibility tests, optimization studies, and performance evaluation of the CONFIDANTE system. Chap. 1 and Chap. 2 present the motivation and basic concepts for CONFIDANTE. In Chap. 3, the concept was tested with ^{252}Cf point sources and PuO$_2$ hemispheres. The first system was based on the design of a previous TEI system with an anti-symmetric mask randomly chosen based on imaging performance in simulation. The ^{252}Cf sources were used to evaluate the system performance for matching point sources, misaligned point sources, and shapes of multiple sizes by placing the point source on a 2-D stage to trace out squares and circles. The PuO$_2$ hemispheres were placed in matching and non-matching configurations to test the system response to extended sources. The feasibility measurement performance was evaluated using Feynman-Y and reduced χ^2 metrics. Results showed that matching objects produced the expected flat distribution with Poisson noise and the non-matching objects exhibited enough modulation to be quantifiably identified. Notably, if images were reconstructed from the non-matching objects, the image revealed the differences between the objects, which was identified as a potential risk to information leakage if a negative result was obtained due to misalignment or mispositioning of the objects. For this reason, the host party would have every incentive to ensure that false negatives were not obtained.

Chap. 4 presented the results of performance optimization studies. First, the shape of the mask, mask elements, and detector was evaluated using the reduced χ^2 metric to examine their effect imaging artifacts. Changing the mask from cylindrical to spherical improved imaging at vertical displacements off the centerline, but changing the shape of individual mask elements or the shape of the detector either did not improve performance. Second, the size and thickness of the mask and size of the detector were evaluated using a new methodology to optimize and evaluate designs. This methodology used the Negative Log-Likelihood (NLL) to calculate true positive and true negative rates for simulated matching and non-matching sources. Its development was motivated

by the need for a metric that was sensitive to the performance to confirm true positives (same objects) and true negatives (different objects) while incorporating the total detection efficiency of the system. In TEI systems it is especially true that the detection efficiency and the imaging performance are at odds, so they both need to be considered in the optimization. A parametric study was completed to evaluate a range of mask thicknesses and detector sizes using simulated sources of rings of different sizes. A thick mask, which offered more modulation, was much better at distinguishing between non-matching objects and was not significantly worse at confirming matching objects. Somewhat surprisingly, the larger detectors also did better, which was attributed to the need for more counts to overcome statistical fluctuations.

Chap. 5 presented the second system. Based on the results from Chap. 4, the mask was 3D-printed. 3D-printing was a practical and convenient method in constrast to the machining challenges of subtractive manufacturing a coded spherical mask. Based on measurements with ^{252}Cf, the spherical shape has the desired improvement to make the response more uniform across the field of view. Measurements were also completed using the ^{252}Cf to trace out multiple sizes of rings to compare with the simulations. The 2.54 cm detector showed the same trends as the simulation except for the matching point sources, for which the measured data performed much better than simulation. Overall, the new system confirmed matching sources and was able to distinguish between sources with more than a 5 cm difference in diameter for a reasonable total number of emitted neutrons.

The combination of the initial proof of concept measurements, parametric simulation optimizations, and confirming measurements using the second generation system provide proof the second system has numerically superior detector capabilities useful to a future deployment.

6.2   Future Work

There are many avenues of future research to extend the design of the CONFIDANTE system. To start, there are several tasks related to improving the current system.

First, one useful set of measurements would be with the sources placed opposite each other during the entire measurement instead of the current method of synthesizing data sets by adding a phase shift to during analysis. The work in this dissertation did not consider how misalignment of the items being measured might affect the measurement results. A host would have incentive to reduce these sorts of errors, as they could lead to false negative or put information at risk, but a study should be conducted to develop an understanding of the tolerances that would be required.

Second, other detector sizes should be tested to see if the simulations accurately predicted that the efficiency gain from a larger detector had more impact on the discrim-

ination performance than the overall image resolution of the system.

Third, there are additional analyses of the measured data that could be performed to examine additional aspects fo the system. For instance, looking at the metrics as a function of the number of counts, analogous to performance as a function of time. It is difficult to tell if a distribution is Poisson if it has less than ten counts per bin, which means at least 3000 counts total are required. Understanding the minimum required time to achieve confidence that numerical results are above or below a given threshold would mature the ConOps. It is also important to check if there is information at risk if matching objects are measured for a long time or the data from multiple measurements is saved.

Fourth, there are potential improvements to the simulation, such as more accurate efficiency estimates for the different detectors. This would improve the ray-tracing without sacrificing the speed of the simulations. Development of MCNP simulations has begun and will be helpful as a more accurate model of the background from scatter as well as being able to model more complex sources of interest. MCNP captures more complexities of a model but is much slower to run. Analyses of metrics from these more complex models would enable more accurate bounds on the performance requirements for procedures and implementation of ConOps.

There are also several avenues of future work related to other types of particles and the electronics of the system. While neutrons are a valuble signature of nuclear weapons material, they do not carry much specificity to the isotopic composition of the emitting material and so may be easier to spoof. CONFIDANTE is sensitive to the volumetric distribution of neutron-emitting material, but because it only depends on integral count rates, there is little way to distinguish between types of neutron emitters. This was the basis for the use of ^{252}Cf and PuO$_2$ as neutron sources for our measurements. A non-weapon grade material would need to have the same intensity and spatial distribution as the weapon-grade material against which it was being tested in order for CONFIDANTE to present a false positive. Methods to distinguish between different spontaneous fission isotopes or (α, n) reactions, such as multiplicity calculations or very fine energy binning, would add complicated data collection and analysis which goes against the motivation for CONFIDANTE as a ZKP systems.

Therefore, a gamma-ray version of the system has been proposed. Since gamma-ray spectra can be used to identify the isotope from which they came, such a system would increase the confidence in a positive measurement. However, the challenges discussed in Section 2.4.1.3 remain: saving a full gamma-ray spectrum would reveal too much information, but using energy windows might provide a path forward.

While much of the code used for CONFIDANTE can be used in the development of a gamma-ray version, there are some notable additions. First, source energy bins were added to the code as the value of gamma detection is that spectroscopy can be used to identify isotopes and the gross integral counts over the entire energy spectrum is not

sufficient. More work will be necessary to understand how to use energy windows to provide enough confidence without putting information at risk. This mask will likely be smaller and thinner than the neutron mask, but will still likely be quite heavy, as the best materials for attenuating gamma rays are tungsten and lead. Fortunately, additive manufacturing through metal laser sintering has been developed to work with tungsten and tungsten alloys, so a spherical mask is an extremely exciting possility[59]. The addition of a collimater inside the mask to limit the field of view to the two objects has been proposed and will also be evaluated in simulation. Design simulations are underway. The goal is to build the gamma system in 2021.

There are also ideas related to the electronics needed to read out a system like CONFIDANTE. In this thesis, much more information was recorded than the final implementation should, as it is useful in the types of analysis performed. One notable change from the first system to the second was removing timing/location information from being recorded and instead operating the system at a set of discrete locations, so that it was read out as binned. In future work we would like to remove the need for some of the complex processors, specifically the digitizer and processing code. By making circuits for different pieces of the data analysis, the goal is to make each piece easier to certify as part of a verification procedure[60]. One piece under development is a PSD circuit. Rather than running analysis on saved waveforms, this circuit would do the PSD analysis inline and output a logic pulse if the event was the desired particle. This output could feed into a simple counter, so then the output would be the total number of neutrons without any other saved information. The concept for this circuit is in the process of being manufactured and tested. Another circuit will be needed to address the energy windows needed for a gamma ray system. Again, recording the entire energy spectrum would likely put too much information at risk, but the total number of counts within certain windows or the ratio between windows has been proposed before. The idea is to have a circuit that could set thresholds and only output pulses with an amplitude that was within the energy range thresholds. When and if these circuits are developed, they could easily be tested by integrating them in the readout chain of CONFIDANTE in place of the digitizer.

The current path seeks to demonstrate the effectiveness of this method by building prototypes of gamma-ray and neutron systems and measuring lab sources and uses simulation to examine the response of the systems to more complicated items of interest. While there is still a lot of work needed before any of these would be ready for implementation in a treaty, there are several interesting and innovative avenues to research that would further the objectives of an arms reduction treaty verification concept.

Bibliography

[1] *Nuclear weapons: Who has what at a glance*, Jul. 2019. [Online]. Available: `https://www.armscontrol.org/factsheets/Nuclearweaponswhohaswhat`.

[2] H. M. Kristensen, R. S. Norris, and M. Korda, *Nuclear Notebook*, https://thebulletin.org/nuclear-notebook, Jan. 2020.

[3] M. Dreicer, F. Dalnoki-Veress, and P. M. Lewis, "Report on the INMM Workshop on Preparing for Nuclear Arms Reductions to Address Technical Transparency and Verification Challenges," *Journal of Nuclear Material Management*, pp. 53–56, 2012.

[4] Defense Science Board, "Assessment of Nuclear Monitoring and Verification Technologies," Department of Defense, Tech. Rep., 2014.

[5] A. Bohlen, W. Burns, S. Pifer, and J. Woodworth, "The Treaty on Intermediate-range Nuclear Forces: History and Lessons Learned," en, Foreign Policy at Brookings, Tech. Rep. 9, Dec. 2012, p. 37.

[6] *Treaty between the united states of america and the russian federation on measures for the further reduction and limitation of strategic offensive arms*, 1968.

[7] Congressional Research Service, "Verifying arms control agreements: The Soviet view : Report," Library of Congress, Tech. Rep., 1987.

[8] P. Sonne, "Top general wants key nuclear pact with Russia expanded to include new weapons," en, *Washington Post*, Feb. 2019.

[9] A. F. Woolf, "The new START treaty: Central limits and key provisions (updated)," Tech. Rep. R41219, 2020, pp. 169–236.

[10] *Treaty between the united states of america and the union of soviet socialist republics on the elimination of their intermediate-range and shorter-range missiles*, Accessed 2020-06-30, 1987. [Online]. Available: `https://www.acq.osd.mil/tc/inf/INFtoc.htm`.

[11] T. J. Crawford, *CMC technology laboratories fact sheet: Radiation detection equipment for monitoring the inf treaty*, 1999.

[12] J. H. McNeilly and B. D. Rothstein, "Radiation Detection Equipment (RDE) Comparative Evaluation Test Program. Volume 1. Point Source Measurements," en, SCIENCE APPLICATIONS INTERNATIONAL CORP NEWINGTON VA CENTER FOR VERIFICATION RESEARCH, Tech. Rep., Aug. 1994, ch. Technical Reports.

[13] J. Yan and A. Glaser, "Nuclear Warhead Verification: A Review of Attribute and Template Systems," en, Tech. Rep., Sep. 2015, pp. 157–170.

[14] M. Hamel, "Next-Generation Arms-Control Agreements Based on Emerging Radiation DetectionTechnologies," in *INMM 59th Annual Meeting*, Baltimore, MD, USA, Jul. 2018.

[15] D. J. Mitchell and K. M. Tolk, "Trusted Radiation Attribute Demonstration System," Sandia National Laboratories, Albuquerque, NM, Tech. Rep. SAND2000-1481C, 2000.

[16] M. R. Smith, "Introduction To the Attribute Verification–Neutron/Gamma (AVNG) Program," in *INMM Annu. Meet.*, 2010.

[17] J. M. Puckett, D. G. Langner, S.-t. Hsue, D. Macarthur, N. J. Nicholas, R. Whiteson, T. B. Gosnell, Z. Koenig, J. Wolford, M. Aparo, I. Kulikov, J. Whichello, V. J. Poplavko, S. Razinkov, and V. Terekhin, "General Technical Requirements and Functional Specifications for an Attribute Measurement System for the Trilateral Initiative," in *INMM Annu. Meet.*, 2001.

[18] E. (Haas, A. Sukhanov, and J. (Murphy, "Trilateral Initiative: IAEA Authentication and National Certification of Verification Equipment for Facilities with Classified Forms of Fissile Materia," in *IAEA Symp. Int. Safeguards Verif. Nucl. Mater. Secur.*, 2001.

[19] T. Ramsøy, E. Day, K. Allen, C. Marsh, M. Morgan-reading, S. Backe, T. Bjerk, S. Hustveit, and S. Høibråten, "United Kingdom - Norway Initiative Information Barrier Development: Technical Trial Results," 2013.

[20] "The United Kingdom-Norway Initiative: further research into the verificaiton of nuclear warhead dismantlement," in *2015 Rev. Conf. Parties to Treaty Non-prolif. Nucl. Weapons*, 2015. [Online]. Available: `https://undocs.org/NPT/CONF.2015/WP.31`.

[21] L. R. Avens, J. E. Doyle, and M. F. Mullen, "The Fissile Material Transparency Technology Demonstration," en, in *INMM 42nd Annual Meeting*, Indian Wells, CA, Jul. 2001, p. 8.

[22] J. Thron, M. Smith, D. W. Macarthur, D. Bracken, L. Carrillo, T. Elmont, N. Johansen, K. Frame, J. Gallegos, P. Karpius, J. Shergur, D. Vo, and R. Williams, "Next Generation Attribute Measurement System," in *INMM Annu. Meet.*, 2007.

[23] P. B. Merkle, T. M. Weber, J. D. Strother, J. Etzkin, A. J. Flynn, J. C. Bartberger, W. C. Amai, and L. F. Anderson, "Next Generation Trusted Radiation Identification System," en, in *INMM Annual Meeting*, 2010, p. 5.

[24] G. Warren, D. Archer, M. Cunningham, S. McConchie, and J. Thron, "Concepts for the Measurements Subsystems of the Third Generation Attributes Measurement System," in *INMM 53rd Annual Meeting*, Orlando, FL, United States, Jul. 2012.

[25] K. D. Seager, D. J. Mitchell, T. W. Laub, K. M. Tolk, R. L. Lucero, and K. W. Insch, "Trusted Radiation Identification System," en, p. 9,

[26] C. Sastre and P. Vanier, "CIVET a Controlled Intrusiveness Verification Technology," en, Tech. Rep. BNL–90156-1988, 970415, Dec. 1988, BNL–90156-1988, 970 415. DOI: 10.2172/970415.

[27] P. B. Zuhoski, P. E. Vanier, and J. P. Indusi, "Building a Dedicated Information Barrier System for Warhead and Sensitive Item Verification," 1999, p. 7.

[28] P. E. Vanier, P. Zuhoski, C. A. Salwen, L. Forman, A. Sviridov, N. Isaev, V. Chebykine, and Y. Seldiakov, "Study of the CIVET Design of a Trusted Processor for Non-intrusive Measurements*," en, p. 12, 2001.

[29] D. E. Archer, C. L. Britton, R. J. Carter, R. F. Lind, J. T. Mihalczo, J. A. Mullens, J. E. Radle, and M. C. Wright, "Fieldable Nuclear Material Identification System," en, in *INMM Annual Meeting*, 2010, p. 8.

[30] S. Goldwasser, S. Micali, and C. Rackoff, "The knowledge complexity of interactive proof systems," *SIAM J. Comput.*, 1989.

[31] J.-J. Quisquater, L. Guillou, and T. Berson, "How to explain zero-knowledge protocols to your childres," 1998.

[32] M. Naor, Y. Naor, and O. Reingold, "Applied Kid Cryptography or How To Convince Your Children You Are Not Cheating," 1999.

[33] A. Glaser, B. Barak, and R. J. Goldston, "A zero-knowledge protocol for nuclear warhead verification," *Nature*, vol. 510, pp. 497–501, 2014. DOI: doi:10.1038/nature13457.

[34] E. B. Sasson, A. Chiesa, C. Garman, M. Green, I. Miers, E. Tromer, and M. Virza, "Zerocash: Decentralized Anonymous Payments from Bitcoin," en, in *2014 IEEE Symposium on Security and Privacy*, San Jose, CA: IEEE, May 2014, pp. 459–474, ISBN: 978-1-4799-4686-0. DOI: 10.1109/SP.2014.36.

[35] M. Blum, P. Feldman, and S. Micali, "Non-Interactive Zero-Knowledge and Its Applications," en, in *Proceedings of the Twentieth Annual ACM Symposium on Theory of Computing*, ser. STOC '88, Chicago, Illinois, USA: Association for Computing Machinery, Jan. 1988, pp. 103–112, ISBN: 978-0-89791-264-8. DOI: 10.1145/62212. 62222.

[36] N. Bitansky, R. Canetti, A. Chiesa, and E. Tromer, "From extractable collision resistance to succinct non-interactive arguments of knowledge, and back again," en, in *Proceedings of the 3rd Innovations in Theoretical Computer Science Conference on - ITCS '12*, Cambridge, Massachusetts: ACM Press, 2012, pp. 326–349, ISBN: 978-1-4503-1115-1. DOI: 10.1145/2090236.2090263.

[37] S. Philippe, R. J. Goldston, A. Glaser, and F. d'Errico, "A physical zero-knowledge object-comparison system for nuclear warhead verification," *Nature Communications*, vol. 7, 2016. DOI: doi:10.1038/ncomms12890.

[38] W. K. Pitts, E. M. Brubaker, A. J. Gilbert, N. R. Hilton, K. D. Jarman, P. A. Marleau, and A. Seifert, "Outcomes of a Workshop on Techniques for Information Protection of Imaging Information," en, in *INMM Annual Meeting*, 2016, p. 11.

[39] R. S. Kemp, A. Danagoulian, R. R. Macdonald, and J. R. Vavrek, "Physical cryptographic verification of nuclear warheads," *Proceedings of the National Academy of Sciences*, vol. 113, no. 31, pp. 8618–8623, 2016. DOI: www.pnas.org/cgi/doi/10. 1073/pnas.1603916113.

[40] J. R. Vavrek, B. S. Henderson, and A. Danagoulian, "Experimental demonstration of an isotope-sensitive warhead verification technique using nuclear resonance fluorescence," *Proceedings of the National Academy of Sciences of the United States of America*, vol. 115, no. 17, pp. 4363–4368, 2018, ISSN: 10916490. DOI: 10.1073/pnas. 1721278115. arXiv: 1712.02904.

[41] J. J. Hecla and A. Danagoulian, "Nuclear disarmament verification via resonant phenomena," *Nature Communications*, vol. 9, 2018. DOI: https://doi.org/10. 1038/s41467-018-03680-4.

[42] E. M. Engel and A. Danagoulian, "A physically cryptographic warhead verification system using neutron induced nuclear resonances," *Nature Communications*, vol. 10, no. 1, 2019, ISSN: 20411723. DOI: 10.1038/s41467-019-12386-0. arXiv: 1907.06978.

[43] P. Marleau and E. Brubaker, "An Implementation of Zero Knowledge Confirmation using a Two- dimensional Time-Encoded Imaging System," pp. 1–15, 2016.

[44] S. Fetter, V. A. Frolov, O. F. Prilutsky, and R. Z. Sagdeev, "Fissile Materials and Weapon Design," *Sci. Glob. Secur.*, vol. 1, pp. 225–302, 1990.

[45] *National nuclear data center*, Accessed 2020-04-29. [Online]. Available: www.nndc. bnl.gov.

[46] S. Fetter and R. Mozley, "Emission and Absorption of Radiation," *Science & Global Security*, vol. 1, pp. 225–302, 1990.

[47] J. Birks, *The Theory and Practice of Scintillation Counting*, English, ser. International Series of Monographs in Electronics and Instrumentation. New York: Pergamon Press, 1964, vol. 27.

[48] M. Monterial, P. Marleau, S. Clarke, and S. Pozzi, "Application of Bayes theorem for pulse shape discrimination," en, *Nuclear Instruments and Methods in Physics Research Section A: Accelerators, Spectrometers, Detectors and Associated Equipment*, vol. 795, pp. 318–324, Sep. 2015, ISSN: 01689002. DOI: 10.1016/j.nima.2015.06.014.

[49] R. H. Dicke, "Scatter-hole cameras for x-rays and gamma rays," *The Astrophysical Journal*, vol. 153, pp. 101–106, 1968.

[50] J. Brennan, E. Brubaker, M. Gerling, P. Marleau, K. McMillan, A. Nowack, N. R.-L. Galloudec, and M.Sweany, "Demonstration of two-dimensional time-encoded imaging of fast neutrons," *Nuclear Instruments and Methods in Physics Research A*, vol. 802, pp. 76–81, 2015. DOI: https://doi.org/10.1016/j.nima.2015.08.076.

[51] J. Bushberg, J. Seibert, and E. Leidholdt, *The Essential Physics of Medical Imaging*. Wolters Kluwer Health, 2011, ISBN: 9780781780575.

[52] L. A. Shepp and Y. Vardi, "Maximum likelihood reconstruction for emission tomography," *IEEE transactions on medical imaging*, vol. 1, no. 2, pp. 113–122, 1982.

[53] R. Brun and F. Rademakers, "ROOT - an object oriented data analysis framework," *Nucl. Inst. & Meth. in Phys. Res. A*, vol. 389, pp. 81–86, 1996. [Online]. Available: http://root.cern.ch.

[54] D. MacArthur, D. Hauck, D. Langner, M. Smith, and J. Thron, "Random Selection as a Confidence-Building Tool," en, in *INMM Annual Meeting*, 2010, p. 6.

[55] J. Brennan, E. Brubaker, M. Gerling, P. Marleau, K. McMillan, A. Nowack, N. R.-L. Galloudec, and M. Sweany, "Demonstration of two-dimensional time-encoded imaging of fast neutrons," en, *Nucl. Inst. Methods Phys. Res. A*, vol. 802, pp. 76–81, Dec. 2015, ISSN: 01689002. DOI: 10.1016/j.nima.2015.08.076.

[56] H. Marouani and M. R. Dagenais, *Internal Clock Drift Estimation in Computer Clusters*, en, https://www.hindawi.com/journals/jcnc/2008/583162/, Research Article, May 2008. DOI: 10.1155/2008/583162.

[57] P. Marleau and E. Brubaker, "An implementation of zero knowledge confirmation using a two- dimensional time-encoded imaging system," pp. 1–15, 2016.

[58] R. McConn, C. Gesh, R. Pagh, R. Rucker, and R. Willams, "Compendium of Material Composition Data for Radiation Transport Modeling," en, Pacific Northwest National Laboratory, Tech. Rep. PNNL-15870 Rev. 1, 2011, p. 375.

[59] Wolfmet, *Gamma and X-ray Collimator Tungsten Components*, en-GB, Feb. 2020.

[60] J. K. Polack, E. Brubaker, M. C. Hamel, R. R. Helguero, D. L. Maierhafer, P. Marleau, E. A. Padilla, and T. M. Weber, "A Modular Approach to Trusted System Design for Arms Control Treaty Verification," en, in *Proceedings of the INMM 61st Annual Meeting*, Jul. 2020, p. 10.

Appendix A

Additional Simulation Results

This appendix contains additional results related to Ch. 5.

The following tables contain the likelihood metrics for pairs of sources corresponding to one detector size and one mask thickness as described in 4.2. For matching objects, on the diagonal, a good value is close to 1.0, indicating data mostly flat with some noise. Off the diagonal, a good value is close to 0.0 because that indicates the differences in non-matching objects was detected. The color is intended to help indicate the better values, where green is good and yellow is bad.

	pt	5cm	10 cm	15 cm	20 cm	25 cm
pt	0.0008	0.5744	0.0288	0	0	0
5 cm		0.996	0.6769	0.0337	0.0001	0
10 cm			0.9973	0.9781	0.7199	0.2638
15 cm				0.9962	0.9881	0.9179
20 cm					0.9964	0.9927
25 cm						0.9976

Table A.1. Table of likelihood values for pairs of objects (indicated by row and column) from simulation of a 10 cm thick spherical mask and a cylindrical detector with height and diameter of 2.54 cm.

	pt	5cm	10 cm	15 cm	20 cm	25 cm
pt	0.0149	0.7772	0.1268	0.0023	0	0
5 cm		0.9968	0.8184	0.1401	0.0062	0
10 cm			0.9979	0.9864	0.8584	0.5368
15 cm				0.9973	0.9921	0.958
20 cm					0.9974	0.9964
25 cm						0.9978

Table A.2. Table of likelihood values for pairs of objects (indicated by row and column) from simulation of a 7.5 cm thick spherical mask and a cylindrical detector with height and diameter of 2.54 cm.

	pt	5cm	10 cm	15 cm	20 cm	25 cm
pt	0.2386	0.9243	0.5292	0.1258	0.0231	0.0054
5 cm		0.9962	0.929	0.5354	0.1839	0.0553
10 cm			0.997	0.9906	0.9469	0.8414
15 cm				0.9959	0.9937	0.9822
20 cm					0.9975	0.9955
25 cm						0.9969

Table A.3. Table of likelihood values for pairs of objects (indicated by row and column) from simulation of a 5 cm thick spherical mask and a cylindrical detector with height and diameter of 2.54 cm.

	pt	5cm	10 cm	15 cm	20 cm	25 cm
pt	0.919	0.9903	0.9569	0.8871	0.794	0.7004
5 cm		0.9963	0.9877	0.9601	0.9069	0.8416
10 cm			0.9962	0.9959	0.9929	0.9828
15 cm				0.997	0.9951	0.9939
20 cm					0.9963	0.9958
25 cm						0.9958

Table A.4. Table of likelihood values for pairs of objects (indicated by row and column) from simulation of a 2.5 cm thick spherical mask and a cylindrical detector with height and diameter of 2.54 cm.

	pt	5cm	10 cm	15 cm	20 cm	25 cm
pt	0	0.0128	0	0	0	0
5 cm		0.984	0.457	0	0	0
10 cm			0.9954	0.8514	0.0181	0
15 cm				0.9961	0.9262	0.2409
20 cm					0.996	0.9754
25 cm						0.9971

Table A.5. Table of likelihood values for pairs of objects (indicated by row and column) from simulation of a 10 cm thick spherical mask and a cylindrical detector with height and diameter of 3.81 cm.

	pt	5cm	10 cm	15 cm	20 cm	25 cm
pt	0	0.1061	0.0008	0	0	0
5 cm		0.993	0.6226	0.0003	0	0
10 cm			0.9976	0.9214	0.1148	0.0003
15 cm				0.997	0.958	0.5067
20 cm					0.9967	0.9862
25 cm						0.9967

Table A.6. Table of likelihood values for pairs of objects (indicated by row and column) from simulation of a 7.5 cm thick spherical mask and a cylindrical detector with height and diameter of 3.81 cm.

	pt	5cm	10 cm	15 cm	20 cm	25 cm
pt	0.004	0.504	0.0485	0	0	0
5 cm		0.9967	0.8436	0.0616	0	0
10 cm			0.9969	0.9693	0.5277	0.0628
15 cm				0.9961	0.9814	0.8308
20 cm					0.9971	0.9928
25 cm						0.9959

Table A.7. Table of likelihood values for pairs of objects (indicated by row and column) from simulation of a 5 cm thick spherical mask and a cylindrical detector with height and diameter of 3.81 cm.

	pt	5cm	10 cm	15 cm	20 cm	25 cm
pt	0.6662	0.9546	0.826	0.482	0.1615	0.0455
5 cm		0.9976	0.9823	0.8387	0.4901	0.2162
10 cm			0.9971	0.9932	0.9632	0.8627
15 cm				0.9959	0.9935	0.982
20 cm					0.9964	0.9963
25 cm						0.9974

Table A.8. Table of likelihood values for pairs of objects (indicated by row and column) from simulation of a 2.5 cm thick spherical mask and a cylindrical detector with height and diameter of 3.81 cm.

	pt	5cm	10 cm	15 cm	20 cm	25 cm
pt	0.000	0.0007	0	0	0	0
5 cm		0.9476	0.2246	0	0	0
10 cm			0.9868	0.5745	0	0
15 cm				0.9936	0.6896	0.0012
20 cm					0.9945	0.9026
25 cm						0.9951

Table A.9. Table of likelihood values for pairs of objects (indicated by row and column) from simulation of a 10 cm thick spherical mask and a cylindrical detector with height and diameter of 5.08 cm.

	pt	5cm	10 cm	15 cm	20 cm	25 cm
pt	0	0.0195	0	0	0	0
5 cm		0.9857	0.464	0	0	0
10 cm			0.9939	0.7652	0.0011	0
15 cm				0.9954	0.8256	0.0268
20 cm					0.9951	0.9493
25 cm						0.9946

Table A.10. Table of likelihood values for pairs of objects (indicated by row and column) from simulation of a 7.5 cm thick spherical mask and a cylindrical detector with height and diameter of 5.08 cm.

	pt	5cm	10 cm	15 cm	20 cm	25 cm
pt	0.0005	0.3011	0.0349	0	0	0
5 cm		0.9965	0.8404	0.0114	0	0
10 cm			0.9968	0.9302	0.0896	0
15 cm				0.9975	0.9533	0.3794
20 cm					0.9967	0.9851
25 cm						0.9967

Table A.11. Table of likelihood values for pairs of objects (indicated by row and column) from simulation of a 5 cm thick spherical mask and a cylindrical detector with height and diameter of 5.08 cm.

	pt	5cm	10 cm	15 cm	20 cm	25 cm
pt	0.5002	0.9122	0.7607	0.2632	0.014	0.0001
5 cm		0.9958	0.9815	0.7274	0.1375	0.0082
10 cm			0.9967	0.9882	0.8668	0.4667
15 cm				0.9968	0.9926	0.9457
20 cm					0.998	0.9954
25 cm						0.9971

Table A.12. Table of likelihood values for pairs of objects (indicated by row and column) from simulation of a 2.5 cm thick spherical mask and a cylindrical detector with height and diameter of 5.08 cm.